Insights to scaling remote plasma sources sustained in NF_3 mixtures

Shuo HuangVladimir VolynetsJames R. HamiltonSangheon Lee, In-Cheol Song, and Siqing LuJonathan TennysonMark J. Kushner

Citation: Journal of Vacuum Science & Technology A: Vacuum, Surfaces, and Films **35**, 031302 (2017); doi: 10.1116/1.4978551

View online: http://dx.doi.org/10.1116/1.4978551

View Table of Contents: http://avs.scitation.org/toc/jva/35/3

Published by the American Vacuum Society

Insights to scaling remote plasma sources sustained in NF_3 mixtures

Shuo Huang[a)]
Department of Electrical Engineering and Computer Science, University of Michigan, 1301 Beal Ave., Ann Arbor, Michigan 48109-2122

Vladimir Volynets[b)]
Samsung Electronics Co., Ltd., 129 Samsung-ro, Yeongtong-gu, Suwon-si, Gyeonggi-do 443-742, South Korea

James R. Hamilton[c)]
Department of Physics and Astronomy, University College London, London WC1E 6BT, United Kingdom

Sangheon Lee,[d)] In-Cheol Song,[e)] and Siqing Lu[f)]
Samsung Electronics Co., Ltd., 129 Samsung-ro, Yeongtong-gu, Suwon-si, Gyeonggi-do 443-742, South Korea

Jonathan Tennyson[g)]
Department of Physics and Astronomy, University College London, London WC1E 6BT, United Kingdom

Mark J. Kushner[h)]
Department of Electrical Engineering and Computer Science, University of Michigan, 1301 Beal Ave., Ann Arbor, Michigan 48109-2122

(Received 22 December 2016; accepted 1 March 2017; published 21 March 2017)

Remote plasma sources (RPSs) are being developed for low damage materials processing during semiconductor fabrication. Plasmas sustained in NF_3 are often used as a source of F atoms. NF_3 containing gas mixtures such as NF_3/O_2 and NF_3/H_2 provide additional opportunities to produce and control desirable reactive species such as F and NO. In this paper, results from computational investigations of RPS sustained in capacitively coupled plasmas are discussed using zero-dimensional global and two-dimensional reactor scale models. A comprehensive reaction mechanism for plasmas sustained in $Ar/NF_3/O_2$ was developed using electron impact cross sections for NF_2 and NF calculated by *ab initio* molecular R-matrix methods. For validation of the reaction mechanism, results from the simulations were compared with optical emission spectroscopy measurements of radical densities. Dissociative attachment and dissociative excitation of NF_x are the major sources of F radicals. The exothermicity from these Franck–Condon dissociative processes is the dominant gas heating mechanism, producing gas temperatures in excess of 1500 K. The large fractional dissociation of the feedstock gases enables a larger variety of end-products. Reactions between NF_x and O atom containing species lead to the formation of NO and N_2O through endothermic reactions facilitated by the gas heating, followed by the formation of NO_2 and FNO from exothermic reactions. The downstream composition in the flowing afterglow is an ion–ion plasma maintained by, in oxygen containing mixtures, $[F^-] \approx [NO^+]$ since NO has the lowest ionization potential and F has the highest electron affinity among the major neutral species. © *2017 American Vacuum Society*. [http://dx.doi.org/10.1116/1.4978551]

I. INTRODUCTION

Remote plasma sources (RPSs) are used in microelectronics fabrication to produce fluxes of radicals for etching and surface passivation while minimizing the damage that may occur by charging, energetic ion bombardment and ultraviolet or vacuum ultraviolet radiation.[1] Due to long flow distances enabling recombination or attachment, grids or other discriminating barriers between the source and the substrate, the flux of charged particles reaching the etching chamber is small and the substrate is exposed dominantly to neutrals. RPS reactors have been used for isotropic etching processes such as resist stripping by plasmas sustained in N_2/O_2 and N_2/H_2 mixtures[2,3] and chemical drying etching of SiO_2 and Si_3N_4 by plasmas sustained in F-containing gas mixtures such as $CF_4/O_2/N_2$ (Ref. 4) and NF_3/O_2.[5]

Nitrogen trifluoride (NF_3) is frequently used in RPS for the ease with which F atoms are produced by dissociative attachment. F atoms are the main etchants of silicon-containing materials such as SiO_2, SiC, and Si_3N_4. RPS sustained only in NF_3 typically limits the reactive fluxes reaching the processing chamber to F, N, and NF_x. RPS sustained in NF_3 gas mixtures increases the variety of reactive species that can be produced and so enables more leverage in optimizing the process. For example, the use of NF_3/O_2 mixtures can selectively increase the etch rate of Si_3N_4 by production of NO which aids in the removal of N atoms from the surface.[5] The production of NO may, however, increase

[a)]Electronic mail: shuoh@umich.edu
[b)]Electronic mail: vladimir.volynets@samsung.com
[c)]Electronic mail: james.hamilton@ucl.ac.uk
[d)]Electronic mail: s2009.lee@samsung.com
[e)]Electronic mail: ic13.song@samsung.com
[f)]Electronic mail: siqing.lu@samsung.com
[g)]Electronic mail: j.tennyson@ucl.ac.uk
[h)]Author to whom correspondence should be addressed; electronic mail: mjkush@umich.edu

roughening of the surface.[6,7] The use of NF_3/N_2 mixtures can selectively increase the etch rate of SiO_2 by aiding in the removal of the O atoms, which in turn enhances the removal of Si through formation of the SiF_x etch product.[8] For certain applications, it may be desirable to separately control, for example, F and N_xO_y fluxes so as to optimize the etch rates of SiO_2, Si_3N_4, and other materials. This separate optimization could, in principle, be performed using pulsed power or pulsed gas sources.

Plasma chemistry models of NF_3 mixtures have been developed to gain insights into scaling of RPS systems. Systems based on RPS for the etching of polysilicon and SiO_2 using NF_3/O_2 mixtures were modeled by Meeks *et al.*[9] and Vosen *et al.*[10] by addressing each component of the system with different levels of detail. The remote plasma source, the transport tube, and the downstream etch chamber were modeled in tandem by a zero-dimensional (0d) well mixed reactor model, a 1d plug flow model, and a two-dimensional (2d) axisymmetric reacting-flow model, respectively, which enabled the investigation of the impact of varying plasma source operating parameters on downstream etch results. The etch rate of polysilicon was found to be transport limited whereas the etch rate of SiO_2 was found to be surface-kinetics limited and depend more on pressure and less on flow rate than the etching of polysilicon. The densities at the exit of a remote plasma source sustained in $Ar/NF_3/N_2$ mixtures were predicted using a zero-dimensional kinetic model and served as input for a one-dimensional model to investigate the dependence of atomic fluorine recombination on operating conditions.[11] An increase in wall temperature accelerated the desorption of atomic fluorine from the walls and increased the mole fraction of atomic fluorine. Increasing the flow rate or decreasing the gas pressure increased the fraction of atomic fluorine by decreasing the residence time or mitigating the volume recombination.

A parallel-plate reactor packed with ferroelectric pellets used for removing NF_3 from exhaust gases in semiconductor processing was computationally investigated by Chang *et al.* using a one-dimensional simulation.[12] The addition of O_2 or H_2 to the exhaust gases significantly attenuated the decomposition of NF_3 due to additional electron energy loss to the dissociation of the additives. The enhancement of the electric field resulting from the high dielectric constant of the ferroelectric pellets favored the decomposition of NF_3.

A dielectric barrier discharge (DBD) used for disposing of perfluorinated compounds was modeled by treating the DBD reactor as a series of discharge regions and nondischarge regions alternately placed along the axis of the reactor.[13] Electron impact and exothermic reactions with N atoms (e.g., $NF_2 + N \rightarrow NF + NF$ and $NF + N \rightarrow N_2 + F$) were found to be the major species responsible for the abatement of NF_x in NF_3/N_2 mixtures. An inductively coupled plasma sustained in Ar/NF_3 and Ar/CF_4 mixtures used for etching Si-containing materials was investigated using a global model in which particle balance equations are solved using the electron energy distribution (EED) functions measured by Langmuir probe.[14] The density of F atoms in Ar/NF_3 was found to be about five times higher than in Ar/CF_4 with the same input power primarily due to the low binding energy and large rate coefficients for dissociative processes of NF_3 compared with CF_4.

In this paper, results from a computational investigation of RPS sustained in NF_3 containing gas mixtures at pressures of less than a few Torr using continuous-wave (CW) power for downstream low-damage etching applications are discussed. A comprehensive reaction mechanism for $Ar/NF_3/O_2$ was developed including electron impact cross sections for NF_2 and NF, which were produced using *ab initio* computational techniques based on the molecular R-matrix method. Two modeling approaches were used—0d global modeling to investigate fundamental reaction mechanisms and reactor scale 2d modeling to address the spatial dynamics of flow through the system. We found that F atoms are mainly created through thermal electrons attaching to NF_3 molecules and electronic excitation leading to dissociation. For power depositions typical of RPS systems, gas temperature excursions can exceed 1500 K, which in turn enable a larger variety of endothermic reactions to occur. The addition of O_2 leads to the formation of FO, NO, NO_2, and FNO species through endothermic and exothermic reactions, which are modulated by the gas temperature. In the downstream afterglow, the highly attaching gas mixture rapidly transitions to an ion–ion plasma. The end products are typically determined by the positive ion having the lowest ionization potential and the negative ion having the largest electron affinity, both of which are the end products of charge exchange reactions. For the NF_3 and O_2 containing gas mixtures investigated here, the terminal ion–ion plasma is composed of $[F^-] \approx [NO^+]$, a result enabled by the high gas temperature and large fractional dissociation that enables the formation of NO.

Descriptions of the models are in Sec. II. Cross sections for electron impact NF_x reactions and the reaction mechanism for plasmas sustained in $Ar/NF_3/O_2$ are described in Sec. III. Experimental measurements and simulation results are compared in Sec. IV. The scaling of RPS based on results from the plug flow mode of the global model is discussed in Sec. V. The plasma properties and radical generation in a RPS sustained in CW capacitively coupled plasma (CCP) based on results from the 2d model are discussed in Sec. VI. Concluding remarks are in Sec. VII.

II. DESCRIPTION OF THE MODELS

Two techniques were used to model the RPS—a global model using a plug flow approximation to address plasma and radical generation, and a 2d model combining fluid and kinetic approaches to address flow and electron kinetics in a RPS produced by a CCP. The global model assists in more rapid development of the reaction mechanism and investigation of the operational parameter space. The 2d model addresses spatially dependent electron heating mechanisms and the dynamics of the flow including back diffusion.

The global model, Global_Kin, is a 0d simulation for plasma chemistry, plasma kinetics, and surface chemistry, described in Ref. 15. The global model is implemented in a

plug-flow mode, whereby integration in time is mapped to integration in space by computing a time dependent flow speed. Assuming a constant pressure, the flow speed is determined by the thermal expansion (or contraction) of the gas due to changes in temperature, changes in gas number density due to electron impact and neutral reactions, limited by requiring the flow to be subsonic. The global model consists of differential equations for the densities of species based on the defined reaction mechanism. The power deposition is specified as a function of position.

With electron impact cross sections and mole fractions of gas species, Boltzmann's equation is solved for EEDs over a wide range of E/N (E and N are the electric field and the gas number density). These EEDs are computed while assuming a negligible ionization degree and so electron–electron collisions are not considered. The non-Maxwellian nature of the EEDs is then addressed.[16] This process produces a table having columns of E/N, average electron energy (or equivalent electron temperature, T_e), and electron impact rate coefficients. If T_e is a monotonic function of E/N, the column of E/N can be thrown away, leaving a lookup table of rate coefficients as a function of T_e. The instantaneous T_e is produced by the electron energy equation. Rate coefficients are then obtained by interpolation of the table, $k_i(T_e)$. The table is periodically updated as mole fractions of species change.

More system specific issues of the downstream etch system were investigated using 2d modeling with the hybrid plasma equipment model (HPEM).[17] The HPEM is a modular simulator that combines fluid and kinetic approaches. In the HPEM, continuity, momentum, and energy equations for all species are solved coincident with Poisson's equation for the electric potential. Use of the HPEM explicitly calculates all modes of power (electron and ion) self-consistently. Electron transport is addressed using fluid equations for bulk electrons and a kinetic Monte Carlo simulation for sheath accelerated secondary electrons, which play an important role in the electron heating mechanism in capacitively coupled plasmas. The same procedure is followed to obtain electron impact rate coefficients for the fluid electrons as described for the global model. Nonlocal electron energy transport is accounted for through the thermal conductivity and convection terms of the electron energy equation that provide an electron temperature as a function of position.

III. CROSS SECTIONS AND REACTION MECHANISM

A. Cross sections for electron impact NF_x reactions

The cross sections for electron impact on NF_3 used in our models are based on the compilation by Lisovskiy *et al.*[18] The cross section for dissociative attachment of NF_3 was extended to higher energies to agree with electron swarm data. In the systems of interest, the NF_3 is heavily (if not totally) dissociated, producing large densities and mole fractions of NF_2 and NF, which in turn requires electron impact cross sections for NF_2 and NF. The electron impact cross sections for NF_2 and NF were calculated using the molecular R-matrix method.[19] The cross sections for electron impact on NF_3 compiled by Lisovskiy *et al.* and for electron impact on NF_2 and NF calculated by the R-matrix method are shown in Fig. 1.

The R-matrix method divides the physical space for the problem of interaction between electron and molecule into two regions—an inner region containing the target molecule and an outer region containing the incident electron. The method solves Schrödinger's equation in the inner region independent of the energy of impact electron and then uses this solution to solve the Schrödinger equation in the outer

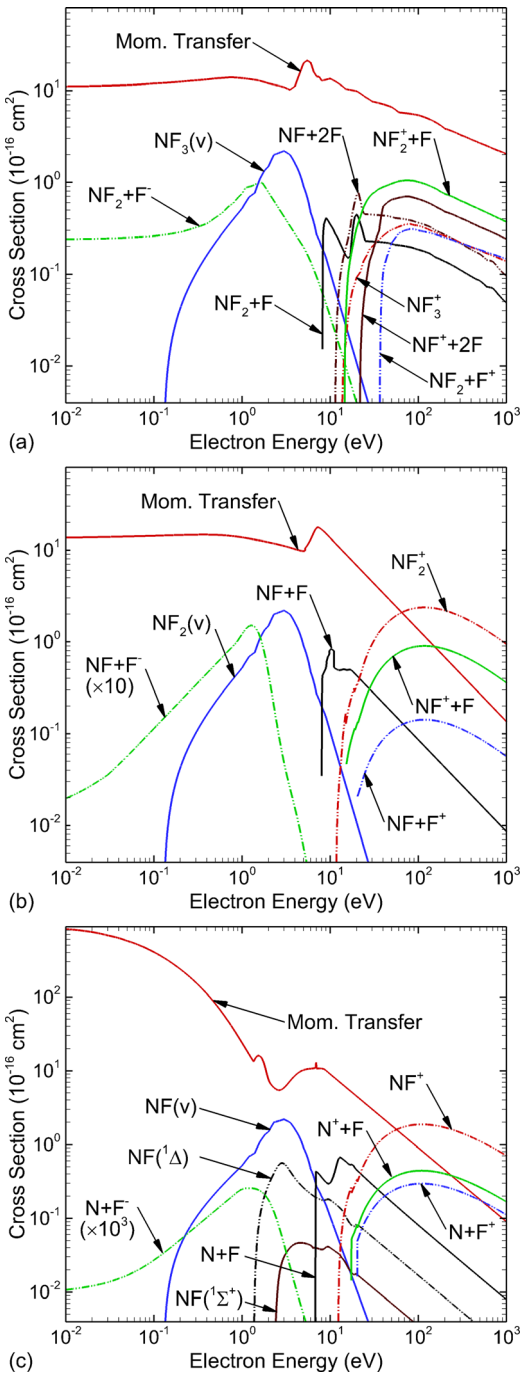

FIG. 1. (Color online) Cross sections for electron impact reactions of (a) NF_3 compiled by Lisovskiy *et al.* (Ref. 18); and (b) NF_2 and (c) NF calculated using the *ab initio* molecular R-matrix method (Ref. 19).

TABLE I. Reaction mechanism for $Ar/NF_3/O_2$ plasmas.

Species[a]						
Ar	$Ar(1s_5)$	$Ar(1s_4)$	$Ar(1s_3)$	$Ar(1s_2)$	Ar(4p)	Ar(4d)
$Ar_2(^3\sum_u^+)$	Ar^+	Ar_2^+	NF_3	NF_2	NF	NF_3^+
NF_2^+	NF^+	N_2	$N_2(v)$	$N_2(A\ ^3\sum_u^+)$	$N_2(B\ ^3\Pi_g$, higher)	
N	$N(^2D)$	N_2^+	N^+	F_2	$F_2(1\ ^1\sum_u^+)$	F
$F(^3S)$	F_2^+	F^+	F^-	O_2	$O_2(v)$	
$O_2(a\ ^1\Delta_g)$	$O_2(b\ ^1\sum_g^+)$	O	$O(^1D)$	$O(^1S)$	O_3	O_2^+
O^+	O_2^-	O^-	O_3^-	FO	FNO	NO
N_2O	NO_2	NO^+	N_2O^+			

Reactions[b] Process	Rate coefficient[c]	References	ΔH (eV)[c]
Electron impact NF_x			
$e + NF_3 \rightarrow NF_3 + e$	[d]	18	[e]
$e + NF_3 \rightarrow NF_2 + F^-$	[d,f]	18	−1.0
$e + NF_3 \rightarrow NF_3(v) + e$	[d,g]	18	
$e + NF_3 \rightarrow NF_2 + F + e$	[d]	18	−5.8
$e + NF_3 \rightarrow NF + F + F + e$	[d]	18	−6.1
$e + NF_3 \rightarrow NF_3^+ + e + e$	[d]	18	
$e + NF_3 \rightarrow NF_2^+ + F + e + e$	[d]	18	−0.5
$e + NF_3 \rightarrow NF^+ + F + F + e + e$	[d]	18	−4.2
$e + NF_3 \rightarrow F^+ + NF_2 + e + e$	[d]	18	−1.1[h]
$e + NF_2 \rightarrow NF_2 + e$	[d]	19	
$e + NF_2 \rightarrow NF + F^-$	[d]	19	−0.5
$e + NF_2 \rightarrow NF_2(v) + e$	[d,g]	19	
$e + NF_2 \rightarrow NF + F + e$	[d]	19	−5.1
$e + NF_2 \rightarrow NF_2^+ + e + e$	[d]	19	
$e + NF_2 \rightarrow NF^+ + F + e + e$	[d]	19	
$e + NF_2 \rightarrow F^+ + NF + e + e$	[d]	19	
$e + NF \rightarrow NF + e$	[d]	19	
$e + NF \rightarrow N + F^-$	[d]	19	−0.6
$e + NF \rightarrow NF(v) + e$	[d,g]	19	
$e + NF \rightarrow NF(^1\Delta) + e$	[d,g]	19	
$e + NF \rightarrow NF(^1\sum^+) + e$	[d,g]	19	
$e + NF \rightarrow N + F + e$	[d]	19	−4.0
$e + NF \rightarrow NF^+ + e + e$	[d]	19	
$e + NF \rightarrow N^+ + F + e + e$	[d]	19	
$e + NF \rightarrow F^+ + N + e + e$	[d]	19	
$e + NF_3^+ \rightarrow NF_2 + F$	$1 \times 10^{-7}\ T_e^{-1/2}$	est. 39[i]	−11.1
$e + NF_2^+ \rightarrow NF + F$	$1 \times 10^{-7}\ T_e^{-1/2}$	est. 39	−6.3[h]
$e + NF^+ \rightarrow N^* + F$	$1 \times 10^{-7}\ T_e^{-1/2}$	est. 39	−7.1
Electron impact F_2/F			
$e + F_2 \rightarrow F_2 + e$	[d]	40	
$e + F_2 \rightarrow F^- + F$	[d]	40	−1.8
$e + F_2 \rightarrow F + F + e$	[d]	40	−1.6
$e + F_2 \rightarrow F_2^* + e$	[d]	40	
$e + F_2 \rightarrow F_2^+ + e + e$	[d]	40	
$e + F_2^+ \rightarrow F + F^*$	$1 \times 10^{-7}\ T_e^{-1/2}$	est. 39	−0.6
$e + F \rightarrow F + e$	[d]	41	
$e + F \rightarrow F^* + e$	[d]	41	
$e + F \rightarrow F^+ + e + e$	[d]	41	
$e + F^* \rightarrow F^+ + e + e$	[d]	41	
$e + F^+ \rightarrow F^*$	$4.5 \times 10^{-13}\ T_e^{-0.5}$	est. 42	
$e + e + F^+ \rightarrow F^* + e$	$5.12 \times 10^{-27}\ T_e^{-4.5}$	est. 42	
Electron impact N_xO_y			
$e + NO \rightarrow NO + e$	[d]	43	
$e + NO \rightarrow N + O^-$	[d]	44	−2.1
$e + NO \rightarrow N + O + e$	[d]	43	−0.3
$e + NO \rightarrow NO^+ + e + e$	[d]	45	
$e + NO \rightarrow N + O^+ + e + e$	[d]	45	−0.1
$e + NO \rightarrow N^+ + O + e + e$	[d]	45	−0.1

TABLE I. (*Continued*)

Reactions[b]			
$e + NO^+ \rightarrow N + O$	$1 \times 10^{-7}\ T_e^{-1/2}$	est. 39	−1.8
$e + NO_2 \rightarrow NO_2 + e$	[d]	46	
$e + NO_2 \rightarrow NO^+ + O + e + e$	[d]	45	−0.5
$e + N_2O \rightarrow N_2O + e$	[d]	47	
$e + N_2O \rightarrow N_2 + O^-$	[d]	47	−0.1
$e + N_2O \rightarrow N_2 + O + e$	[d]	47	−0.2
$e + N_2O \rightarrow N_2O^+ + e + e$	[d]	47 and 48[j]	
$e + N_2O \rightarrow N_2 + O^+ + e$	[d]	47 and 48[j]	
$e + N_2O \rightarrow N_2^+ + O + e$	[d]	47 and 48[j]	
$e + N_2O^+ \rightarrow N_2 + O^*$	$1 \times 10^{-7}\ T_e^{-1/2}$	est. 39	−7.0
Radiative transitions			
$F_2^* \rightarrow F_2$	$2.44 \times 10^7\ s^{-1}$	49	
$F^* \rightarrow F$	$5 \times 10^7\ s^{-1}$	50	
Collisional quenching			
$N_2(v) + M \rightarrow N_2 + M$	2×10^{-15}	51	−0.3
$N_2^* + M \rightarrow N_2 + M$	3×10^{-16}	52	−6.2
$N_2^{**} + M \rightarrow N_2^* + M$	3×10^{-16}	est. 52	−2.2
$N^* + M \rightarrow N + M$	2×10^{-14}	52	−2.4
$O_2(v) + M \rightarrow O_2 + M$	$1 \times 10^{-14}\ T_n^{1/2}$	53	−0.2
$O_2^* + M \rightarrow O_2 + M$	$3 \times 10^{-18} \exp(-200/T_g)$	54	−1.0
$O_2^{**} + M \rightarrow O_2^* + M$	$3.6 \times 10^{-17}\ T_n^{1/2}$	53	−0.6
$O_2^{**} + M \rightarrow O_2 + M$	$4 \times 10^{-18}\ T_n^{1/2}$	53	−1.6
$O^* + M \rightarrow O + M$	5×10^{-12}	25	−1.9
$O(^1S) + M \rightarrow O^* + M$	$4.8 \times 10^{-12} \exp(-850/T_g)$	54	−2.3
$F_2^* + M \rightarrow F_2 + M$	3×10^{-18}	est. 54	−2.0
$F^* + M \rightarrow F + M$	3×10^{-18}	est. 54	−2.0
Penning ionization			
$Ar^* + F_2^* \rightarrow F_2^+ + Ar + e$	$1.2 \times 10^{-9}\ T_n^{1/2}$	est. 27[k]	
$Ar^* + F^* \rightarrow F^+ + Ar + e$	$1.2 \times 10^{-9}\ T_n^{1/2}$	est. 27	
$Ar^* + N_2^* \rightarrow N_2^+ + Ar + e$	$1.2 \times 10^{-9}\ T_n^{1/2}$	est. 27	
$Ar^* + N_2^{**} \rightarrow N_2^+ + Ar + e$	$1.2 \times 10^{-9}\ T_n^{1/2}$	est. 27	
$Ar^* + O_2^* \rightarrow O_2^+ + Ar + e$	$1.2 \times 10^{-9}\ T_n^{1/2}$	est. 27	
$Ar^* + O_2^{**} \rightarrow O_2^+ + Ar + e$	$1.2 \times 10^{-9}\ T_n^{1/2}$	est. 27	
$Ar^* + O(^1S) \rightarrow O^+ + Ar + e$	$1.2 \times 10^{-9}\ T_n^{1/2}$	est. 27	
$Ar^* + NO \rightarrow NO^+ + Ar + e$	$1.2 \times 10^{-9}\ T_n^{1/2}$	est. 27	
$Ar(4p) + N^* \rightarrow N^+ + Ar + e$	$1.2 \times 10^{-9}\ T_n^{1/2}$	est. 27	
$Ar(4d) + N^* \rightarrow N^+ + Ar + e$	$1.2 \times 10^{-9}\ T_n^{1/2}$	est. 27	
$Ar(4p) + O_2 \rightarrow O_2^+ + Ar + e$	$1.2 \times 10^{-9}\ T_n^{1/2}$	est. 27	
$Ar(4d) + O_2 \rightarrow O_2^+ + Ar + e$	$1.2 \times 10^{-9}\ T_n^{1/2}$	est. 27	
$Ar(4p) + O_2(v) \rightarrow O_2^+ + Ar + e$	$1.2 \times 10^{-9}\ T_n^{1/2}$	est. 27	
$Ar(4d) + O_2(v) \rightarrow O_2^+ + Ar + e$	$1.2 \times 10^{-9}\ T_n^{1/2}$	est. 27	
$Ar(4p) + O^* \rightarrow O^+ + Ar + e$	$1.2 \times 10^{-9}\ T_n^{1/2}$	est. 27	
$Ar(4d) + O^* \rightarrow O^+ + Ar + e$	$1.2 \times 10^{-9}\ T_n^{1/2}$	est. 27	
$Ar(4p) + NF_2 \rightarrow NF_2^+ + Ar + e$	$1.2 \times 10^{-9}\ T_n^{1/2}$	est. 27	
$Ar(4d) + NF_2 \rightarrow NF_2^+ + Ar + e$	$1.2 \times 10^{-9}\ T_n^{1/2}$	est. 27	
$Ar(4p) + NF \rightarrow NF^+ + Ar + e$	$1.2 \times 10^{-9}\ T_n^{1/2}$	est. 27	
$Ar(4d) + NF \rightarrow NF^+ + Ar + e$	$1.2 \times 10^{-9}\ T_n^{1/2}$	est. 27	
$Ar(4p) + N_2O \rightarrow N_2O^+ + Ar + e$	$1.2 \times 10^{-9}\ T_n^{1/2}$	est. 27	
$Ar(4d) + N_2O \rightarrow N_2O^+ + Ar + e$	$1.2 \times 10^{-9}\ T_n^{1/2}$	est. 27	
$Ar(4d) + N \rightarrow N^+ + Ar + e$	$1.2 \times 10^{-9}\ T_n^{1/2}$	est. 27	
$Ar(4d) + NF_3 \rightarrow NF_3^+ + Ar + e$	$1.2 \times 10^{-9}\ T_n^{1/2}$	est. 27	
$Ar(4d) + O \rightarrow O^+ + Ar + e$	$1.2 \times 10^{-9}\ T_n^{1/2}$	est. 27	
$Ar_2^* + F_2^* \rightarrow F_2^+ + Ar + Ar + e$	$5.0 \times 10^{-10}\ T_n^{1/2}$	est. 24	
$Ar_2^* + F^* \rightarrow F^+ + Ar + Ar + e$	$5.0 \times 10^{-10}\ T_n^{1/2}$	est. 24	
$Ar_2^* + N_2^* \rightarrow N_2^+ + Ar + Ar + e$	$5.0 \times 10^{-10}\ T_n^{1/2}$	est. 24	
$Ar_2^* + N_2^{**} \rightarrow N_2^+ + Ar + Ar + e$	$5.0 \times 10^{-10}\ T_n^{1/2}$	est. 24	
$Ar_2^* + NO \rightarrow NO^+ + Ar + Ar + e$	$5.0 \times 10^{-10}\ T_n^{1/2}$	est. 24	
$Ar_2^* + O_2^{**} \rightarrow O_2^+ + Ar + Ar + e$	$5.0 \times 10^{-10}\ T_n^{1/2}$	est. 24	
$Ar_2^* + O(^1S) \rightarrow O^+ + Ar + Ar + e$	$5.0 \times 10^{-10}\ T_n^{1/2}$	est. 24	

TABLE I. (*Continued*)

Reactions[b]			
Positive ion−neutral collisions			
$F^+ + F \rightarrow F + F^+$	1×10^{-9}	est. 28[l]	[m]
$F^+ + Ar \rightarrow F + Ar^+$	1×10^{-11}	est.	−1.4
$F^+ + F_2 \rightarrow F + F_2^+$	1×10^{-11}	est.	−1.7
$F^+ + N_2 \rightarrow F + N_2^+$	9.7×10^{-10}	55	−1.8
$F^+ + N_2(v) \rightarrow F + N_2^+$	9.7×10^{-10}	est. 55	−2.1
$F^+ + N \rightarrow F + N^+$	1×10^{-11}	est.	−2.9
$F^+ + O \rightarrow F + O^+$	1×10^{-10}	56	−3.8
$F^+ + NF_3 \rightarrow F + NF_3^+$	1×10^{-11}	est.	−3.9
$F^+ + N_2O \rightarrow F + N_2O^+$	1×10^{-11}	est.	−4.5
$F^+ + NF \rightarrow F + NF^+$	1×10^{-11}	est.	−5.1
$F^+ + O_2 \rightarrow F + O_2^+$	7.01×10^{-10}	55	−5.3
$F^+ + O_2(v) \rightarrow F + O_2^+$	7.01×10^{-10}	est. 55	−5.5
$F^+ + NF_2 \rightarrow F + NF_2^+$	1×10^{-11}	est.	−5.8
$F^+ + NO \rightarrow F + NO^+$	8.64×10^{-10}	55	−8.1
$F^+ + Ar_2^* \rightarrow F + Ar_2^+$	1×10^{-11}	est.	−13.6
$F^+ + NO \rightarrow O + NF^+$	9.4×10^{-11}	55	−1.9
$F^+ + O_2 \rightarrow FO + O^+$	6.06×10^{-11}	55	−1.0
$F^+ + O_2(v) \rightarrow FO + O^+$	6.06×10^{-11}	est. 55	−1.2
$Ar^+ + F_2 \rightarrow Ar + F_2^+$	1×10^{-11}	est.	−0.3
$Ar^+ + N_2 \rightarrow Ar + N_2^+$	1×10^{-11}	est.	−0.4
$Ar^+ + N_2(v) \rightarrow Ar + N_2^+$	1×10^{-11}	est.	−0.7
$Ar^+ + N \rightarrow Ar + N^+$	1×10^{-11}	est.	−1.5
$Ar^+ + O \rightarrow Ar + O^+$	1×10^{-11}	est.	−2.4
$Ar^+ + NF_3 \rightarrow Ar + NF_3^+$	1×10^{-11}	est.	−2.5
$Ar^+ + N_2O \rightarrow Ar + N_2O^+$	1×10^{-11}	est.	−3.1
$Ar^+ + NF \rightarrow Ar + NF^+$	1×10^{-11}	est.	−3.7
$Ar^+ + O_2 \rightarrow Ar + O_2^+$	5.1×10^{-11}	28	−3.9
$Ar^+ + O_2(v) \rightarrow Ar + O_2^+$	5.1×10^{-11}	est. 28	−4.1
$Ar^+ + NF_2 \rightarrow Ar + NF_2^+$	1×10^{-11}	est.	−4.4
$Ar^+ + NO \rightarrow Ar + NO^+$	1×10^{-11}	est.	−6.7
$F_2^+ + F_2 \rightarrow F_2 + F_2^+$	1×10^{-9}	est.	
$F_2^+ + N_2 \rightarrow F_2 + N_2^+$	1×10^{-11}	est.	−0.1
$F_2^+ + N_2(v) \rightarrow F_2 + N_2^+$	1×10^{-11}	est.	−0.4
$F_2^+ + N \rightarrow F_2 + N^+$	1×10^{-11}	est.	−1.2
$F_2^+ + O \rightarrow F_2 + O^+$	1×10^{-11}	est.	−2.1
$F_2^+ + NF_3 \rightarrow F_2 + NF_3^+$	1×10^{-11}	est.	−2.2
$F_2^+ + N_2O \rightarrow F_2 + N_2O^+$	1×10^{-11}	est.	−2.8
$F_2^+ + NF \rightarrow F_2 + NF^+$	1×10^{-11}	est.	−3.4
$F_2^+ + O_2 \rightarrow F_2 + O_2^+$	1×10^{-11}	est.	−3.6
$F_2^+ + O_2(v) \rightarrow F_2 + O_2^+$	1×10^{-11}	est.	−3.8
$F_2^+ + NF_2 \rightarrow F_2 + NF_2^+$	1×10^{-11}	est.	−4.1
$F_2^+ + NO \rightarrow F_2 + NO^+$	1×10^{-11}	est.	−6.4
$F_2^+ + Ar_2^* \rightarrow F_2 + Ar_2^+$	1×10^{-11}	est.	−11.9
$N_2^+ + N_2 \rightarrow N_2 + N_2^+$	1×10^{-9}	est.	
$N_2^+ + N_2(v) \rightarrow N_2 + N_2^+$	1×10^{-9}	est.	−0.3
$N_2^+ + N \rightarrow N_2 + N^+$	8.0×10^{-12}	57	−1.1
$N_2^+ + O \rightarrow N_2 + O^+$	9.8×10^{-12}	55	−2.0
$N_2^+ + NF_3 \rightarrow N_2 + NF_3^+$	1×10^{-11}	est.	−2.1
$N_2^+ + N_2O \rightarrow N_2 + N_2O^+$	6×10^{-10}	58	−2.7
$N_2^+ + NF \rightarrow N_2 + NF^+$	1×10^{-11}	est.	−3.3
$N_2^+ + O_2 \rightarrow N_2 + O_2^+$	5×10^{-11}	55	−3.5
$N_2^+ + O_2(v) \rightarrow N_2 + O_2^+$	5×10^{-11}	est. 55	−3.7
$N_2^+ + NF_2 \rightarrow N_2 + NF_2^+$	1×10^{-11}	est.	−4.0
$N_2^+ + NO \rightarrow N_2 + NO^+$	4.1×10^{-10}	55	−6.3
$N_2^+ + Ar_2^* \rightarrow N_2 + Ar_2^+$	1×10^{-11}	est.	−11.8
$N_2^+ + N_2O \rightarrow N_2 + N + NO^+$	4×10^{-10}	58	−1.4
$N_2^+ + NO_2 \rightarrow N_2O + NO^+$	5×10^{-11}	58	−4.8
$N_2^+ + O_2 \rightarrow NO + NO^+$	1×10^{-17}	59	−4.5

TABLE I. (*Continued*)

Reactions[b]			
$N_2^+ + O_2(v) \rightarrow NO + NO^+$	1×10^{-17}	est. 59	−4.7
$N_2^+ + O \rightarrow N + NO^+$	1.4×10^{-10}	58	−3.1
$N_2^+ + O \rightarrow N^* + NO^+$	$1.8 \times 10^{-10}\ T_n^{-1}$	58	−0.7
$Ar_2^+ + N \rightarrow Ar + Ar + N^+$	1×10^{-11}	est.	−0.2
$Ar_2^+ + O \rightarrow Ar + Ar + O^+$	1×10^{-11}	est.	−1.1
$Ar_2^+ + NF_3 \rightarrow Ar + Ar + NF_3^+$	1×10^{-11}	est.	−1.2
$Ar_2^+ + N_2O \rightarrow Ar + Ar + N_2O^+$	1×10^{-11}	est.	−1.8
$Ar_2^+ + NF \rightarrow Ar + Ar + NF^+$	1×10^{-11}	est.	−2.4
$Ar_2^+ + O_2 \rightarrow Ar + Ar + O_2^+$	1×10^{-11}	est.	−2.6
$Ar_2^+ + O_2(v) \rightarrow Ar + Ar + O_2^+$	1×10^{-11}	est.	−2.8
$Ar_2^+ + NF_2 \rightarrow Ar + Ar + NF_2^+$	1×10^{-11}	est.	−3.1
$Ar_2^+ + NO \rightarrow Ar + Ar + NO^+$	1×10^{-11}	est.	−5.4
$N^+ + N \rightarrow N + N^+$	1×10^{-9}	est.	
$N^+ + O \rightarrow N + O^+$	1×10^{-11}	est.	−0.9
$N^+ + NF_3 \rightarrow N + NF_3^+$	1×10^{-11}	est.	−1.0
$N^+ + N_2O \rightarrow N + N_2O^+$	1×10^{-11}	est.	−1.6
$N^+ + NF \rightarrow N + NF^+$	1×10^{-11}	est.	−2.2
$N^+ + O_2 \rightarrow N + O_2^+$	3.07×10^{-10}	55	−2.4
$N^+ + O_2(v) \rightarrow N + O_2^+$	3.07×10^{-10}	est. 55	−2.6
$N^+ + NF_2 \rightarrow N + NF_2^+$	1×10^{-11}	est.	−2.9
$N^+ + NO \rightarrow N + NO^+$	4.72×10^{-10}	55	−5.2
$N^+ + Ar_2^* \rightarrow N + Ar_2^+$	1×10^{-11}	est.	−10.7
$N^+ + N_2O \rightarrow N_2 + NO^+$	5.5×10^{-10}	58	−10.1
$N^+ + NO \rightarrow O + N_2^+$	8.33×10^{-11}	60	−2.1
$N^+ + O_2 \rightarrow NO + O^+$	4.64×10^{-11}	55	−2.4
$N^+ + O_2(v) \rightarrow NO + O^+$	4.64×10^{-11}	est. 55	−2.6
$N^+ + O_2 \rightarrow O + NO^+$	2.32×10^{-10}	55	−6.6
$N^+ + O_2(v) \rightarrow O + NO^+$	2.32×10^{-10}	est. 55	−6.8
$O^+ + O \rightarrow O + O^+$	1×10^{-9}	est.	
$O^+ + NF_3 \rightarrow O + NF_3^+$	1×10^{-11}	est.	−0.1
$O^+ + N_2O \rightarrow O + N_2O^+$	6.3×10^{-10}	58	−0.7
$O^+ + NF \rightarrow O + NF^+$	1×10^{-11}	est.	−1.3
$O^+ + O_2 \rightarrow O + O_2^+$	2.1×10^{-11}	55	−1.5
$O^+ + O_2(v) \rightarrow O + O_2^+$	2.1×10^{-11}	est. 55	−1.7
$O^+ + NF_2 \rightarrow O + NF_2^+$	1×10^{-11}	est.	−2.0
$O^+ + NO \rightarrow O + NO^+$	8×10^{-13}	55	−4.3
$O^+ + Ar_2^* \rightarrow O + Ar_2^+$	1×10^{-11}	est.	−9.8
$O^+ + N_2 \rightarrow N + NO^+$	1.2×10^{-12}	55	−1.0
$O^+ + N_2(v) \rightarrow N + NO^+$	1.2×10^{-12}	est. 55	−1.3
$O^+ + N_2O \rightarrow NO + NO^+$	2.3×10^{-10}	58	−5.9
$O^+ + N_2O \rightarrow N_2 + O_2^+$	2×10^{-11}	58	−5.0
$O^+ + O_3 \rightarrow O_2 + O_2^+$	1×10^{-10}	61	−5.6
$NF_3^+ + NF_3 \rightarrow NF_3 + NF_3^+$	1×10^{-9}	est.	
$NF_3^+ + N_2O \rightarrow NF_3 + N_2O^+$	1×10^{-11}	est.	−0.6
$NF_3^+ + NF \rightarrow NF_3 + NF^+$	1×10^{-11}	est.	−1.2
$NF_3^+ + O_2 \rightarrow NF_3 + O_2^+$	1×10^{-11}	est.	−1.4
$NF_3^+ + O_2(v) \rightarrow NF_3 + O_2^+$	1×10^{-11}	est.	−1.6
$NF_3^+ + NF_2 \rightarrow NF_3 + NF_2^+$	1×10^{-11}	est.	−1.9
$NF_3^+ + NO \rightarrow NF_3 + NO^+$	1×10^{-11}	est.	−4.2
$NF_3^+ + Ar_2^* \rightarrow NF_3 + Ar_2^+$	1×10^{-11}	est.	−9.7
$N_2O^+ + N_2O \rightarrow N_2O + N_2O^+$	1×10^{-9}	est.	
$N_2O^+ + NF \rightarrow N_2O + NF^+$	1×10^{-11}	est.	−0.6
$N_2O^+ + O_2 \rightarrow N_2O + O_2^+$	2.24×10^{-10}	58	−0.8
$N_2O^+ + O_2(v) \rightarrow N_2O + O_2^+$	2.24×10^{-10}	est. 58	−1.0
$N_2O^+ + NF_2 \rightarrow N_2O + NF_2^+$	1×10^{-11}	est.	−1.3
$N_2O^+ + NO \rightarrow N_2O + NO^+$	2.3×10^{-10}	est. 58	−3.6
$N_2O^+ + Ar_2^* \rightarrow N_2O + Ar_2^+$	1×10^{-11}	est.	−9.1
$N_2O^+ + N_2O \rightarrow N_2 + NO + NO^+$	1.2×10^{-11}	58	−3.5
$N_2O^+ + NO_2 \rightarrow N_2 + O_2 + NO^+$	4.29×10^{-10}	58	−3.8

TABLE I. (*Continued*)

Reactions[b]			
$N_2O^+ + O_2 \rightarrow NO_2 + NO^+$	4.59×10^{-11}	58	−3.2
$NF^+ + NF \rightarrow NF + NF^+$	1×10^{-9}	est.	
$NF^+ + O_2 \rightarrow NF + O_2^+$	1×10^{-11}	est.	−0.2
$NF^+ + O_2(v) \rightarrow NF + O_2^+$	1×10^{-11}	est.	−0.4
$NF^+ + NF_2 \rightarrow NF + NF_2^+$	1×10^{-11}	est.	−0.7
$NF^+ + NO \rightarrow NF + NO^+$	1×10^{-11}	est.	−3.0
$NF^+ + Ar_2^* \rightarrow NF + Ar_2^+$	1×10^{-11}	est.	−8.5
$NF^+ + NF_3 \rightarrow NF_2 + NF_2^+$	5.5×10^{-10}	62	−0.9
$O_2^+ + O_2 \rightarrow O_2 + O_2^+$	1×10^{-9}	est.	
$O_2^+ + O_2(v) \rightarrow O_2 + O_2^+$	1×10^{-9}	est.	−0.2
$O_2^+ + NF_2 \rightarrow O_2 + NF_2^+$	1×10^{-11}	est.	−0.5
$O_2^+ + NO \rightarrow O_2 + NO^+$	4.6×10^{-10}	55	−2.8
$O_2^+ + Ar_2^* \rightarrow O_2 + Ar_2^+$	1×10^{-11}	est.	−8.3
$O_2^+ + N \rightarrow O + NO^+$	1.5×10^{-10}	55	−4.1
$O_2^+ + N_2 \rightarrow NO + NO^+$	1×10^{-17}	59	−0.9
$O_2^+ + N_2(v) \rightarrow NO + NO^+$	1×10^{-17}	est. 59	−1.2
$NF_2^+ + NF_2 \rightarrow NF_2 + NF_2^+$	1×10^{-9}	est.	
$NF_2^+ + NO \rightarrow NF_2 + NO^+$	1×10^{-11}	est.	−2.3
$NF_2^+ + Ar_2^* \rightarrow NF_2 + Ar_2^+$	1×10^{-11}	est.	−7.8
$NO^+ + NO \rightarrow NO + NO^+$	1×10^{-9}	est.	
$NO^+ + Ar_2^* \rightarrow NO + Ar_2^+$	1×10^{-11}	est.	−5.5
Negative ion−neutral collisions			
$F^- + F \rightarrow F_2 + e$	1.4×10^{-10}	est. 63	
$O_3^- + O \rightarrow O_2 + O_2 + e$	1.1×10^{-13}	64	
$O_3^- + F \rightarrow F^- + O_3$	5.5×10^{-10}	est. 64	−1.3
$O_3^- + O \rightarrow O_2^- + O_2$	1×10^{-11}	64	−2.5
$O^- + N_2 \rightarrow N_2O + e$	1×10^{-12}	58	
$O^- + N_2(v) \rightarrow N_2O + e$	1×10^{-12}	est. 58	
$O^- + N \rightarrow NO + e$	2.2×10^{-10}	65	
$O^- + NO \rightarrow NO_2 + e$	2.1×10^{-10}	66	
$O^- + O_2 \rightarrow O_3 + e$	5×10^{-15}	64	
$O^- + O_2(v) \rightarrow O_3 + e$	5×10^{-15}	est. 64	
$O^- + O_2^{**} \rightarrow O + O_2 + e$	$6.9 \times 10^{-10}\ T_n^{1/2}$	61	
$O^- + O \rightarrow O_2 + e$	1.4×10^{-10}	63	
$O^- + O_3 \rightarrow O_2 + O_2 + e$	2×10^{-14}	64	
$O^- + F \rightarrow F^- + O$	5.5×10^{-10}	est. 64	−1.9
$O^- + O_2 \rightarrow O_2^- + O$	2.5×10^{-14}	67	1.0
$O^- + O_2(v) \rightarrow O_2^- + O$	2.5×10^{-14}	est. 67	0.8
$O^- + O_3 \rightarrow O_3^- + O$	5.5×10^{-10}	64	−0.6
$O^- + O_3 \rightarrow O_2^- + O_2$	1×10^{-11}	64	−3.0
$O_2^- + N \rightarrow NO_2 + e$	4×10^{-10}	65	
$O_2^- + O_2^* \rightarrow O_2 + O_2 + e$	2×10^{-10}	68	
$O_2^- + O \rightarrow O_3 + e$	$1.5 \times 10^{-10}\ T_n^{1/2}$	28	
$O_2^- + F \rightarrow F^- + O_2$	5.5×10^{-10}	est. 64	−2.9
$O_2^- + N_2O \rightarrow O_3^- + N_2$	1×10^{-11}	58	−1.0
$O_2^- + O_2 \rightarrow O_3^- + O$	3×10^{-15}	69	2.5
$O_2^- + O_2(v) \rightarrow O_3^- + O$	3×10^{-15}	est. 69	2.3
$O_2^- + O \rightarrow O^- + O_2$	$1.5 \times 10^{-10}\ T_n^{1/2}$	28	−1.0
$O_2^- + O_3 \rightarrow O_3^- + O_2$	3.2×10^{-10}	64	−1.6
Ion−ion neutralization			
$F^- + F_2^+ \rightarrow F + F_2^*$	2×10^{-7}	est. 29[n]	−4.4
$F^- + F^+ \rightarrow F + F^*$	2×10^{-7}	est.	−1.0
$F^- + NF_3^+ \rightarrow F + NF_2 + F$	2×10^{-7}	est.	−7.5
$F^- + NF_2^+ \rightarrow F + NF + F$	2×10^{-7}	est.	−2.6[h]
$F^- + NF^+ \rightarrow F + N + F$	1×10^{-7}	est.	−5.8
$F^- + NF^+ \rightarrow F + N^* + F$	1×10^{-7}	est.	−3.4
$F^- + N_2^+ \rightarrow F + N_2^*$	2×10^{-7}	est.	−0.3
$F^- + N^+ \rightarrow F + N^*$	2×10^{-7}	est.	−0.2
$F^- + O_2^+ \rightarrow F + O_2^*$	2×10^{-7}	est.	

TABLE I. (*Continued*)

Reactions[b]			
$F^- + O^+ \rightarrow F + O^*$	2×10^{-7}	est.	−0.7
$F^- + NO^+ \rightarrow F + NO$	2×10^{-7}	est.	−0.4[h]
$F^- + N_2O^+ \rightarrow F + N_2O$	$2 \times 10^{-7}\ T_n^{-1/2}$	est. 58	−9.5
$F^- + N_2O^+ \rightarrow F + N_2 + O$	1×10^{-7}	est. 58	−7.7
$F^- + Ar^+ \rightarrow F + Ar(1s_5)$	1×10^{-7}	est.	−1.0
$F^- + Ar^+ \rightarrow F + Ar(1s_3)$	1×10^{-7}	est.	−0.9
$F^- + Ar_2^+ \rightarrow F + Ar + Ar$	2×10^{-7}	est.	−11.3
$O^- + F_2^+ \rightarrow O + F_2^*$	2×10^{-7}	est.	−1.3
$O^- + F^+ \rightarrow O + F^*$	2×10^{-7}	est.	
$O^- + NF_3^+ \rightarrow O + NF_2 + F$	2×10^{-7}	est.	−9.4
$O^- + NF_2^+ \rightarrow O + NF + F$	2×10^{-7}	est.	−4.5[h]
$O^- + NF^+ \rightarrow O + N^* + F$	2×10^{-7}	est.	−5.3
$O^- + N_2^+ \rightarrow O + N_2^*$	2×10^{-7}	est.	−2.2
$O^- + N^+ \rightarrow O + N^*$	2×10^{-7}	est.	
$O^- + O_2^+ \rightarrow O + O_2^*$	2×10^{-7}	est.	−0.2
$O^- + O^+ \rightarrow O + O^*$	2×10^{-7}	est.	
$O^- + NO^+ \rightarrow O + NO$	2×10^{-7}	est.	[h]
$O^- + N_2O^+ \rightarrow O + N_2O$	$2 \times 10^{-7}\ T_n^{-1/2}$	58	−11.4
$O^- + N_2O^+ \rightarrow O + N_2 + O$	1×10^{-7}	58	−9.6
$O^- + Ar^+ \rightarrow O + Ar(1s_5)$	1×10^{-7}	est.	−2.9
$O^- + Ar^+ \rightarrow O + Ar(1s_3)$	1×10^{-7}	est.	−2.8
$O^- + Ar_2^+ \rightarrow O + Ar + Ar$	2×10^{-7}	est.	−13.2
$O_3^- + F_2^+ \rightarrow O_3 + F_2^*$	2×10^{-7}	est.	−0.7
$O_3^- + F^+ \rightarrow O_3 + F^*$	2×10^{-7}	est.	−0.5
$O_3^- + NF_3^+ \rightarrow O_3 + NF_2 + F$	2×10^{-7}	est.	−8.8
$O_3^- + NF_2^+ \rightarrow O_3 + NF + F$	2×10^{-7}	est.	−3.9[h]
$O_3^- + NF^+ \rightarrow O_3 + N^* + F$	2×10^{-7}	est.	−4.7
$O_3^- + N_2^+ \rightarrow O_3 + N_2^*$	2×10^{-7}	est.	−0.6
$O_3^- + N^+ \rightarrow O_3 + N^*$	2×10^{-7}	est.	
$O_3^- + O_2^+ \rightarrow O_3 + O_2^*$	$2 \times 10^{-7}\ T_n^{-1/2}$	64	−0.5
$O_3^- + O^+ \rightarrow O_3 + O^*$	$1 \times 10^{-7}\ T_n^{-1/2}$		−0.5
$O_3^- + NO^+ \rightarrow O_3 + NO$	2×10^{-7}	est.	−0.7[h]
$O_3^- + N_2O^+ \rightarrow O_3 + N_2O$	$2 \times 10^{-7}\ T_n^{-1/2}$	58	−10.8
$O_3^- + N_2O^+ \rightarrow O_3 + N_2 + O$	1×10^{-7}	58	−9.0
$O_3^- + Ar^+ \rightarrow O_3 + Ar(1s_5)$	1×10^{-7}	est.	−2.3
$O_3^- + Ar^+ \rightarrow O_3 + Ar(1s_3)$	1×10^{-7}	est.	−2.2
$O_3^- + Ar_2^+ \rightarrow O_3 + Ar + Ar$	2×10^{-7}	est.	−12.6
$O_2^- + F_2^+ \rightarrow O_2 + F_2^*$	2×10^{-7}	est.	−0.2
$O_2^- + F^+ \rightarrow O_2 + F^*$	2×10^{-7}	est.	
$O_2^- + NF_3^+ \rightarrow O_2 + NF_2 + F$	2×10^{-7}	est.	−10.4
$O_2^- + NF_2^+ \rightarrow O_2 + NF + F$	2×10^{-7}	est.	−5.5[h]
$O_2^- + NF^+ \rightarrow O_2 + N^* + F$	2×10^{-7}	est.	−6.3
$O_2^- + N_2^+ \rightarrow O_2 + N^* + N^*$	2×10^{-7}	est.	−0.5
$O_2^- + N^+ \rightarrow O_2 + N^*$	2×10^{-7}	est.	−0.5
$O_2^- + O_2^+ \rightarrow O_2 + O_2^*$	2×10^{-7}	est.	−0.4
$O_2^- + O^+ \rightarrow O_2 + O^*$	2×10^{-7}	est.	
$O_2^- + NO^+ \rightarrow O_2 + NO$	1×10^{-7}	est.	−0.5[h]
$O_2^- + NO^+ \rightarrow O_2 + N + O$	1×10^{-7}	58	−2.2
$O_2^- + N_2O^+ \rightarrow O_2 + N_2O$	$2 \times 10^{-7}\ T_n^{-1/2}$	58	−12.4
$O_2^- + N_2O^+ \rightarrow O_2 + N_2 + O$	1×10^{-7}	58	−10.6
$O_2^- + Ar^+ \rightarrow O_2 + Ar(1s_5)$	1×10^{-7}	est.	−3.9
$O_2^- + Ar^+ \rightarrow O_2 + Ar(1s_3)$	1×10^{-7}	est.	−3.8
$O_2^- + Ar_2^+ \rightarrow O_2 + Ar + Ar$	2×10^{-7}	est.	−14.2
Neutral–neutral collisions			
$O_2 + O_2 \rightarrow O_3 + O$	$1.11 \times 10^{-11} \exp(-49\,800/T_g)$	70	4.1
$O_2 + O_2(v) \rightarrow O_3 + O$	$1.11 \times 10^{-11} \exp(-47\,481/T_g)$	70	3.9
$O_2(v) + O_2(v) \rightarrow O_3 + O$	$1.11 \times 10^{-11} \exp(-45\,162/T_g)$	70	3.7
$O_2 + O_2^* \rightarrow O + O_3$	2.95×10^{-21}	est. 71	3.1
$O_2(v) + O_2^* \rightarrow O + O_3$	2.95×10^{-21}	est. 71	2.9

TABLE I. (*Continued*)

Reactions[b]			
$O_2 + O^* \rightarrow O + O_2^{**}$	$2.56 \times 10^{-11} \exp(-67/T_g)$	53	−0.3
$O_2 + O^* \rightarrow O + O_2^{*}$	$1.6 \times 10^{-12} \exp(-67/T_g)$	53	−0.9
$O_2(v) + O^* \rightarrow O + O_2^{**}$	2.56×10^{-11}	est. 53	−0.5
$O_2(v) + O^* \rightarrow O + O_2^{*}$	1.6×10^{-12}	est. 53	−1.1
$O_2^{*} + O_2^{*} \rightarrow O_2 + O_2$	$9 \times 10^{-17} \exp(-560/T_g)$	54	−2.0
$O_2^{*} + O_2^{*} \rightarrow O_2^{**} + O_2$	$9 \times 10^{-17} \exp(-560/T_g)$	54	−0.4
$O_2^{*} + O(^1S) \rightarrow O^* + O_2^{**}$	2.9×10^{-11}	61	−1.7
$O_2^{*} + O(^1S) \rightarrow O + O_2$	1.1×10^{-10}	est. 61	−5.2
$O_2^{*} + O(^1S) \rightarrow O + O + O$	3.2×10^{-11}	61	
$O_2^{*} + O_3 \rightarrow O_2 + O_2 + O$	$5.2 \times 10^{-11} \exp(-2840/T_g)$	63	0.1
$O_2^{**} + O_2^{**} \rightarrow O_2^{*} + O_2$	$3.6 \times 10^{-17} T_n^{0.5}$	est. 72	−2.2
$O_2^{**} + O_3 \rightarrow O + O_2 + O_2$	1.5×10^{-11}	63	−0.5
$O + O_3 \rightarrow O_2 + O_2$	$8.71 \times 10^{-12} \exp(-2113/T_g)$	73	−4.1
$O + O_3 \rightarrow O_2^{*} + O_2$	$1 \times 10^{-11} \exp(-2300/T_g)$	63	−3.1
$O^* + O_3 \rightarrow O_2 + O_2$	1.2×10^{-10}	72	−6.0
$O^* + O_3 \rightarrow O_2 + O + O$	1.2×10^{-10}	72	−0.8
$O(^1S) + O_3 \rightarrow O_2 + O_2$	5.8×10^{-10}	74	−8.3
$O_3 + O_3 \rightarrow O_2 + O_2 + O_2$	$7.42 \times 10^{-12} \exp(-9460/T_g)$	75	−3.0
$N_2^{*} + N \rightarrow N_2 + N^*$	$4 \times 10^{-11} T_n^{-0.66}$	52	−3.8
$N_2^{**} + N \rightarrow N_2 + N^*$	$4 \times 10^{-11} T_n^{-0.66}$	est. 52	−6.0
$N_2 + O_2 \rightarrow NO + NO$	$9.85 \times 10^{-6} \exp(-64\,660/T_g)$	76	1.8
$N_2 + O_2(v) \rightarrow NO + NO$	$9.85 \times 10^{-6} \exp(-62\,341/T_g)$	est. 76	1.6
$N_2(v) + O_2 \rightarrow NO + NO$	$9.85 \times 10^{-6} \exp(-61\,180/T_g)$	est. 76	1.5
$N_2(v) + O_2(v) \rightarrow NO + NO$	$9.85 \times 10^{-6} \exp(-58\,861/T_g)$	est. 76	1.3
$N_2 + O \rightarrow N + NO$	$1.26 \times 10^{-10} \exp(-38\,040/T_g)$	73	3.2
$N_2(v) + O \rightarrow N + NO$	$1.26 \times 10^{-10} \exp(-34\,560/T_g)$	est. 73	2.9
$N_2 + O_2 \rightarrow N_2O + O$	$1 \times 10^{-10} \exp(-55\,200/T_g)$	59	3.5
$N_2 + O_2(v) \rightarrow N_2O + O$	$1 \times 10^{-10} \exp(-52\,881/T_g)$	est. 59	3.3
$N_2(v) + O_2 \rightarrow N_2O + O$	$1 \times 10^{-10} \exp(-51\,722/T_g)$	est. 59	3.2
$N_2(v) + O_2(v) \rightarrow N_2O + O$	$1 \times 10^{-10} \exp(-49\,403/T_g)$	est. 59	3.0
$N_2^{*} + O_2 \rightarrow N_2O + O$	7.8×10^{-14}	59	−2.7
$N_2^{*} + O_2 \rightarrow N_2O + O^*$	3×10^{-14}	59	−0.8
$N_2^{*} + O_2(v) \rightarrow N_2O + O$	7.8×10^{-14}	est. 59	−2.9
$N_2^{*} + O_2(v) \rightarrow N_2O + O^*$	3×10^{-14}	est. 59	−1.0
$N_2^{*} + O_2 \rightarrow N_2 + O_2^{*}$	$2 \times 10^{-13} T_n^{0.55}$	61	−5.0
$N_2^{*} + O_2 \rightarrow N_2 + O_2^{**}$	$2 \times 10^{-12} T_n^{0.55}$	61	−4.0
$N_2^{*} + O_2(v) \rightarrow N_2 + O_2^{*}$	$2 \times 10^{-13} T_n^{0.55}$	est. 61	−5.2
$N_2^{*} + O_2(v) \rightarrow N_2 + O_2^{**}$	$2 \times 10^{-12} T_n^{0.55}$	est. 61	−4.2
$N_2^{*} + O \rightarrow NO + N$	5×10^{-10}	59	−3.0
$N_2^{*} + O \rightarrow NO + N^*$	1×10^{-12}	59	−0.6
$N_2^{*} + O_3 \rightarrow NO + NO + O$	8.4×10^{-12}	59	−0.3
$N_2^{**} + O \rightarrow NO + N$	5×10^{-10}	77	−3.0
$N_2^{**} + O_3 \rightarrow NO + NO + O$	8.4×10^{-12}	59	−3.3
$N + O_2 \rightarrow NO + O$	$4.4 \times 10^{-12} T_n \exp(-3270/T_g)$	78	−1.4
$N + O_2(v) \rightarrow NO + O$	$4.4 \times 10^{-12} T_n \exp(-951/T_g)$	est. 78	−1.6
$N + O_2^{*} \rightarrow NO + O$	$2 \times 10^{-14} \exp(-600/T_g)$	59	−2.4
$N + O_2^{**} \rightarrow NO + O$	2.5×10^{-10}	79	−3.0
$N + O_3 \rightarrow NO + O_2$	5×10^{-16}	80	−5.5
$N^* + O_2 \rightarrow NO + O$	$1.22 \times 10^{-11} \exp(-317/T_g)$	81	−3.8
$N^* + O_2 \rightarrow NO + O^*$	$6 \times 10^{-12} T_n^{0.5}$	58	−1.9
$N^* + O_2(v) \rightarrow NO + O$	1.22×10^{-11}	est. 81	−4.0
$N^* + O_2(v) \rightarrow NO + O^*$	$6 \times 10^{-12} T_n^{0.5}$	est. 58	−2.1
$N^* + O_2^{*} \rightarrow NO + O$	2×10^{-14}	est. 59	−4.8
$N^* + O_2^{**} \rightarrow NO + O$	2.5×10^{-10}	est. 79	−5.4
$N^* + O_3 \rightarrow NO + O_2$	1×10^{-10}	59	−7.9
$N + NO_2 \rightarrow NO + NO$	1.33×10^{-12}	59	−3.4
$N + NO_2 \rightarrow N_2 + O + O$	1.12×10^{-12}	76	
$N + NO_2 \rightarrow N_2 + O_2$	1.41×10^{-12}	73	−5.2
$N + NO_2 \rightarrow N_2O + O$	$5.8 \times 10^{-12} \exp(220/T_g)$	58	−1.7

TABLE I. (*Continued*)

Reactions[b]			
$N + NO \rightarrow N_2 + O$	3.14×10^{-11}	82	−3.2
$N^* + NO_2 \rightarrow NO + NO$	1.5×10^{-12}	83	−5.8
$N^* + NO_2 \rightarrow N_2 + O + O$	1.12×10^{-12}	est. 76	−2.4
$N^* + NO_2 \rightarrow N_2 + O_2$	1.41×10^{-12}	est. 73	−7.6
$N^* + NO_2 \rightarrow N_2O + O$	$1.5 \times 10^{-12} \exp(-570/T_g)$	59	−4.1
$N^* + NO \rightarrow N_2 + O$	6.3×10^{-11}	83	−5.6
$NO + O \rightarrow N + O_2$	$7.48 \times 10^{-13} T_n \exp(-19\,500/T_g)$	73	1.4
$NO + O^* \rightarrow O_2 + N$	1.5×10^{-10}	84	−0.5
$NO + O_3 \rightarrow O_2 + NO_2$	$1.4 \times 10^{-12} \exp(-1310/T_g)$	85	−2.1
$NO + NO \rightarrow N_2 + O_2$	$1.35 \times 10^{-11} \exp(-28\,680/T_g)$	75	−1.8
$NO + NO \rightarrow N_2O + O$	$7.22 \times 10^{-12} \exp(-33\,155/T_g)$	59	1.7
$NO_2 + O \rightarrow O_2 + NO$	$6.5 \times 10^{-12} \exp(120/T_g)$	59	−2.0
$NO_2 + O^* \rightarrow O_2 + NO$	3×10^{-10}	59	−3.9
$NO_2 + NO_2 \rightarrow NO + NO + O_2$	$2.63 \times 10^{-11} \exp(-13\,790/T_g)$	73	1.2
$N_2O + N_2^* \rightarrow O + N_2 + N_2$	8×10^{-11}	58	−4.5
$N_2O + N_2^* \rightarrow NO + N + N_2$	8×10^{-11}	58	−1.3
$N_2O + N^* \rightarrow N_2 + NO$	$1.5 \times 10^{-11} \exp(-570/T_g)$	58	−7.3
$N_2O + O \rightarrow N_2 + O_2$	$1.66 \times 10^{-10} \exp(-14\,100/T_g)$	59	−3.5
$N_2O + O \rightarrow NO + NO$	$1.15 \times 10^{-10} \exp(-13\,400/T_g)$	59	−1.7
$N_2O + O^* \rightarrow N_2 + O_2$	4.93×10^{-11}	59	−5.4
$N_2O + O^* \rightarrow N_2 + O_2^*$	$2.43 \times 10^{-12} TN_n^{2.3} \exp(-9645/T_g)$	86	−4.4
$N_2O + O^* \rightarrow NO + NO$	8.22×10^{-11}	59	−3.6
$N_2O + NO \rightarrow NO_2 + N_2$	$2.92 \times 10^{-13} TN_n^{2.23} \exp(-23\,292/T_g)$	59	−1.5
$F_2 + O \rightarrow F + FO$	$1.62 \times 10^{-11} \exp(-5233/T_g)$	73	−0.7
$F + O_3 \rightarrow FO + O_2$	$2.82 \times 10^{-11} \exp(-252/T_g)$	73	−1.2
$FO + O \rightarrow O_2 + F$	5×10^{-11}	87	−2.9
$FO + O^* \rightarrow O_2 + F$	5×10^{-11}	88	−4.8
$FO + F \rightarrow F_2 + O$	$6.61 \times 10^{-14} \exp(-9561/T_g)$	73	0.7
$NF_3 + N \rightarrow NF + NF_2$	$2.13 \times 10^{-12} T_n^{1.97} \exp(-15\,120/T_g)$	89	−0.5
$NF_2 + N \rightarrow NF + NF$	3.0×10^{-12}	90	−0.1
$NF_2 + N \rightarrow N_2 + F + F$	$1.4 \times 10^{-11} \exp(-95/T_g)$	91	−3.7
$NF + N \rightarrow N_2 + F$	2.5×10^{-10}	est. 92	−6.7
$NF_3 + N^* \rightarrow NF + NF_2$	2.13×10^{-12}	est. 89	−2.9
$NF_2 + N^* \rightarrow NF + NF$	3.0×10^{-12}	est. 90	−2.5
$NF_2 + N^* \rightarrow N_2 + F + F$	1.4×10^{-11}	est. 91	−6.1
$NF + N^* \rightarrow N_2 + F$	2.5×10^{-10}	92	−9.1
$NF_3 + NF \rightarrow NF_2 + NF_2$	1×10^{-14}	93	−0.4
$NF_2 + NF_2 \rightarrow NF + NF_3$	$1.66 \times 10^{-12} \exp(-18\,600/T_g)$	94	0.4
$NF + NF \rightarrow N_2 + F + F$	$6.88 \times 10^{-11} \exp(-1251/T_g)$	76	−3.6
$NF + NF \rightarrow N_2 + F_2$	4×10^{-12}	76	−5.2
$NF_2 + F_2 \rightarrow F + NF_3$	$3.0 \times 10^{-14} \exp(-4860/T_g)$	95	−1.0
$NF_3 + O^* \rightarrow NF_2 + FO$	1.1×10^{-11}	96	−1.6
$NF_2 + O \rightarrow NF + FO$	1.79×10^{-12}	90	0.7
$NF_2 + O \rightarrow F + FNO$	1.25×10^{-11}	90	−2.9
$NF_2 + FO \rightarrow FNO + F + F$	3.8×10^{-12}	97	−0.6
$NF_2 + NO_2 \rightarrow FNO + FNO$	$8.6 \times 10^{-14} \exp(-2444/T_g)$	98	−2.1
$F_2 + NO \rightarrow F + FNO$	1.2×10^{-14}	99	−0.8
$FO + NO \rightarrow F + NO_2$	2.6×10^{-11}	87	−0.9
$FO + FO \rightarrow F + F + O_2$	2.09×10^{-12}	73	−0.6
$FNO + O \rightarrow F + NO_2$	3.0×10^{-13}	100	−0.8
High temperature chemistry			
$F_2 + M \rightarrow F + F + M$	$7.6 \times 10^{-12} \exp(-14\,300/T_g)$	101	1.6
$F_2^* + M \rightarrow F + F + M$	7.6×10^{-12}	est. 101	−11.3
$FO + M \rightarrow F + O + M$	$1.31 \times 10^{-10} \exp(-52\,740/T_g)$	est. 102	2.3
$FNO + M \rightarrow F + NO + M$	$1.31 \times 10^{-10} \exp(-53\,899/T_g)$	est. 102	2.4
$N_2 + M \rightarrow N + N + M$	$9.86 \times 10^{-5} T_n^{-3.33} \exp(-113\,220/T_g)$	103	9.8
$N_2(v) + M \rightarrow N + N + M$	$9.86 \times 10^{-5} T_n^{-3.33} \exp(-109\,740/T_g)$	est. 103	9.5
$N_2^* + M \rightarrow N + N + M$	$9.86 \times 10^{-5} T_n^{-3.33} \exp(-41\,337/T_g)$	est. 103	3.6
$N_2^* + M \rightarrow N^* + N + M$	$9.86 \times 10^{-5} T_n^{-3.33} \exp(-69\,163/T_g)$	est. 103	6.0

TABLE I. (*Continued*)

Reactions[b]			
$N_2^{**} + M \rightarrow N + N + M$	$9.86 \times 10^{-5}\ T_n^{-3.33} \exp(-41\,337/T_g)$	est. 103	3.6
$N_2^{**} + M \rightarrow N^* + N + M$	$9.86 \times 10^{-5}\ T_n^{-3.33} \exp(-69\,163/T_g)$	est. 103	6.0
$NF_3 + M \rightarrow NF_2 + F + M$	$3.98 \times 10^{-10} \exp(-18\,417/T_g)$	104	2.6
$NF_2 + M \rightarrow NF + F + M$	$1.26 \times 10^{-9} \exp(-25\,700/T_g)$	105	3.0
$NF + M \rightarrow N + F + M$	$1.31 \times 10^{-10} \exp(-52\,740/T_g)$	est. 102	3.1
$NO + M \rightarrow N + O + M$	$2.28 \times 10^{-10} \exp(-74\,680/T_g)$	102	6.6
$NO_2 + M \rightarrow NO + O + M$	$1.88 \times 10^{-4}\ T_n^{-3.37} \exp(-37\,640/T_g)$	106	3.2
$N_2O + M \rightarrow N_2 + O + M$	$2.36 \times 10^{-10} \exp(-25\,810/T_g)$	71	1.8
$O_2 + M \rightarrow O + O + M$	$1.31 \times 10^{-10} \exp(-52\,740/T_g)$	102	5.2
$O_2(v) + M \rightarrow O + O + M$	$1.31 \times 10^{-10} \exp(-50\,422/T_g)$	est. 102	5.0
$O_2^* + M \rightarrow O + O + M$	$1.31 \times 10^{-10} \exp(-41\,146/T_g)$	est. 102	4.2
$O_2^{**} + M \rightarrow O + O + M$	$1.31 \times 10^{-10} \exp(-34\,190/T_g)$	est. 102	3.6
$O_3 + M \rightarrow O_2 + O + M$	$7.17 \times 10^{-10} \exp(-11\,170/T_g)$	102	1.1
$F + F + M \rightarrow F_2 + M$	$2.8 \times 10^{-34}\ cm^6\ s^{-1}$	101	−1.6
$F + F + M \rightarrow F_2^* + M$	$2.8 \times 10^{-34} \exp(-131\,012/T_g)\ cm^6\ s^{-1}$	est. 101	11.3
$F + O + M \rightarrow FO + M$	$1.0 \times 10^{-33}\ cm^6\ s^{-1}$	107	−2.3
$F + NO + M \rightarrow FNO + M$	$5.9 \times 10^{-32}\ T_n^{-1.7}\ cm^6\ s^{-1}$	108	−2.4
$N + N + M \rightarrow N_2 + M$	$1.41 \times 10^{-32}\ cm^6\ s^{-1}$	73	−9.8
$N + N + M \rightarrow N_2(v) + M$	$1.41 \times 10^{-32}\ cm^6\ s^{-1}$	est. 73	−9.5
$N^* + N + M \rightarrow N_2^* + M$	$1.41 \times 10^{-32}\ cm^6\ s^{-1}$	est. 73	−6.0
$N + N + M \rightarrow N_2^* + M$	$1.41 \times 10^{-32}\ cm^6\ s^{-1}$	est. 73	−3.6
$N^* + N + M \rightarrow N_2^{**} + M$	$1.41 \times 10^{-32}\ cm^6\ s^{-1}$	est. 73	−6.0
$N + N + M \rightarrow N_2^{**} + M$	$1.41 \times 10^{-32}\ cm^6\ s^{-1}$	est. 73	−3.6
$NF_2 + F + M \rightarrow NF_3 + M$	$1.03 \times 10^{-30}\ cm^6\ s^{-1}$	109	−2.6
$NF + F + M \rightarrow NF_2 + M$	$1.03 \times 10^{-30}\ cm^6\ s^{-1}$	est. 109	−3.0
$N + F + M \rightarrow NF + M$	$2.8 \times 10^{-34}\ cm^6\ s^{-1}$	est. 101	−3.1
$N + O + M \rightarrow NO + M$	$9.13 \times 10^{-33}\ cm^6\ s^{-1}$	73	−6.6
$NO + O + M \rightarrow NO_2 + M$	$1.0 \times 10^{-31}\ T_n^{-1.6}\ cm^6\ s^{-1}$	85	−3.2
$O^* + N_2 + M \rightarrow N_2O + M$	$2.8 \times 10^{-36}\ cm^6\ s^{-1}$	85	−3.7
$O + O + M \rightarrow O_2 + M$	$5.25 \times 10^{-35} \exp(906/T_g)\ cm^6\ s^{-1}$	73	−5.2
$O + O + M \rightarrow O_2(v) + M$	$5.25 \times 10^{-35}\ cm^6\ s^{-1}$	est. 73	−5.4
$O + O + M \rightarrow O_2^* + M$	$5.25 \times 10^{-35}\ cm^6\ s^{-1}$	est. 73	−6.2
$O + O + M \rightarrow O_2^{**} + M$	$5.25 \times 10^{-35}\ cm^6\ s^{-1}$	est. 73	−6.8
$O + O_2 + M \rightarrow O_3 + M$	$2.57 \times 10^{-35} \exp(-855/T_g)\ cm^6\ s^{-1}$	76	−1.1

[a]For simplicity in the reaction list, following notation is used for excited states: $Ar_2^* \leftrightarrow Ar_2(^3\sum_u^+)$, $N_2^* \leftrightarrow N_2(A\ ^3\sum_u^+)$, $N_2^{**} \leftrightarrow N_2(B^3\Pi_g$, higher), $N^* \leftrightarrow N(^2D)$, $F_2^* \leftrightarrow F_2(1\ ^1\sum_u^+)$, $F^* \leftrightarrow F(^3S)$, $O_2^* \leftrightarrow O_2(a\ ^1\Delta_g)$, $O_2^{**} \leftrightarrow O_2(b\ ^1\sum_g^+)$, and $O^* \leftrightarrow O(^1D)$.

[b]This table is a subset of the mechanism for $Ar/NF_3/O_2$ plasmas. The reactions that would occur in a pure Ar discharge are the same as discussed in Ref. 24. The electron impact reactions and radiative transitions that would occur in a pure O_2 plasma and a pure N_2 plasma are the same as discussed in Refs. 25 and 26, respectively.

[c]Rate coefficients have units of $cm^3\ s^{-1}$ unless noted. T_e is electron temperature (eV). T_g is gas temperature (K) and T_n is normalized gas temperature (T_g/300 K). ΔH is the change of the enthalpy (eV).

[d]Rate coefficients are calculated from the electron energy distributions produced by solutions of Boltzmann's equation using electron impact cross sections. The cross section is for the forward reaction. Reverse cross sections are obtained by detailed balance.

[e]The rate of gas heating by elastic collisions is $k_m(3/2)k_B(2\,m_e/M)(T_e - T_g)$ eV cm^3/s, for elastic rate coefficient k_m, electron mass m_e, neutral mass M, and Boltzmann's constant k_B.

[f]The cross section for dissociative attachment of NF_3 from Ref. 18 was modified so as to agree with the electron swarm data.

[g]Electron impact excitation of NF_x to the vibrationally excited states, $NF_3(v)$, $NF_2(v)$, and NF(v), and the electronically excited states, $NF(^1\Delta)$ and $NF(^1\sum^+)$, was treated by assuming ground state NF_x as the final product with an energy loss of the activation energy.

[h]Reduced gas heating was assumed. Actual product would be the transient excited state with higher potential energy which rapidly decays to states with lower potential energy by emitting a photon.

[i]Rate coefficient for dissociative recombination was assumed to be $1 \times 10^{-7}\ cm^3\ s^{-1}$ (Ref. 39) when measured or calculated data is not available.

[j]The total ionization cross section is from Ref. 47, branching ratio from Ref. 48.

[k]Ar^* represents any excited atomic state of Ar. The same Penning ionization rate coefficient was used for all pairings of excited states of Ar.

[l]Rate coefficient for charge exchange between ions and neutrals was assumed to be $1 \times 10^{-11}\ cm^3\ s^{-1}$ ($1 \times 10^{-9}\ cm^3\ s^{-1}$ for resonant charge exchange) (Ref. 28) when measured or calculated data are not available.

[m]The rate of gas heating of the neutral by charge exchange is $k_{ce}(3/2)k_B(T_{ion} - T_g)$ eV cm^3/s, for charge exchange rate coefficient k_{ce} and ion temperature T_{ion}.

[n]Rate coefficient for neutralization between positive and negative ions was assumed to be $2 \times 10^{-7}\ cm^3 s^{-1}$ (Ref. 29) when measured or calculated data is not available.

region, which is energy dependent. The cross sections for electron impact processes including elastic scattering, dissociative attachment, dissociative excitation, and ionization were calculated using the molecular geometries provided by the National Institute of Standards and Technology (NIST) database.[20,21] All cross sections were calculated using the R-matrix method from threshold to 20 eV. Above 20 eV, the cross section for dissociative attachment goes to 0, while the cross sections for other processes were extrapolated to higher energies using the scaled Born cross sections (for excitation and ionization)[22] or assuming dominant dipole transition (for other processes) and scaling with $\ln(\varepsilon)/\varepsilon$, where ε is the electron energy. The detailed R-matrix method used for calculation of the NF_x cross sections is described in Ref. 23.

B. Reaction mechanism for $Ar/NF_3/O_2$

A reaction mechanism was developed for plasmas sustained in gas mixtures containing $Ar/NF_3/O_2$. The species included in the model are listed in Table I. The rate coefficients for heavy particle collisions are listed in Arrhenius form while the rate coefficients for electron impact reactions were calculated based on the EEDs produced by solutions of Boltzmann's equation as described above. The reactions that would occur in a pure Ar plasma are the same as discussed in Ref. 24. The electron impact reactions and radiative transitions that would occur in a pure O_2 plasma are the same as discussed in Ref. 25 and in a pure N_2 plasmas are the same as discussed in Ref. 26. The additional reactions required to complete the mechanism for $Ar/NF_3/O_2$ are electron impact with NF_x, F_2, F, and N_xO_y and heavy particle reactions in $Ar/NF_3/O_2$ mixtures. These additional reactions are in Table I. The resulting reaction mechanism is intended to be as complete as practical for a discharge sustained in $Ar/NF_3/O_2$ mixtures. As such, there are rate coefficients whose values have never been experimentally or analytically determined, and so a subset of the reaction rate coefficients were estimated based on enthalpies of reactions and analogy with similar reactions. For example, the rate coefficient for Penning ionization between excited states of Ar was uniformly estimated to be $1.2\times10^{-9}\ T_n^{1/2}\ cm^3\ s^{-1}$,[27] the rate coefficient for charge exchange between ions and neutrals was assumed to be $1\times10^{-11}\ cm^3\ s^{-1}$ ($1\times10^{-9}\ cm^3\ s^{-1}$ for resonant charge exchange),[28] and the rate coefficient for neutralization between positive and negative ions was assumed to be $2\times10^{-7}\ cm^3\ s^{-1}$.[29] As to the ion–ion neutralization involving diatomic or polyatomic anions, the rate coefficients can be calculated based on semianalytic expressions.[30]

Although vibrationally excited $NF_x(v)$ is not included as a separate species in the mechanism, electron energy losses for collisions with NF_x producing vibrational states are included. As the gas mixture for our conditions is highly dissociated, the fractional dissociation and density of atomic species are sensitive to the sticking coefficient and recombination probability at the surface of the wall. In this mechanism, the wall recombination coefficients for atomic F, N, and O were uniformly assumed to be 0.01.

NF_3 has a thermal dissociative electron attachment cross section enabled by the electron affinity of F (3.4 eV) being larger than the binding energy of NF_3 ($D_0 = 2.4$ eV).[31] The large rate coefficient of this process results in the dissociation of NF_3 being predominantly due to thermal attachment when the electron temperature is only a few eV. Electronic excitation of NF_3 also leads to dissociation of NF_3 producing NF_2, NF, and F. NF_2 and NF are also thermally attaching species with a binding energy of 2.9 eV (Ref. 31) and 2.8 eV (Ref. 32) producing F^-. These radicals are also dissociated to NF, N, and F through electronic excitation.

In a pure NF_3 discharge, thermodynamically the reaction pathway is terminated by forming N_2 and F_2 through wall recombination and gas phase reactions, although electron impact excitation, dissociation and ionization of these species also occurs. With the addition of O_2 to NF_3, a variety of additional reactions are enabled, which diversifies the species produced in the discharge. O_2 is dissociated into O atoms through electron impact dissociative excitation and attachment. In addition to dissociative processes, electron impact excitation to $O_2(a^1\Delta_g, b^1\sum_g^+)$ and $O(^1D, {}^1S)$ produces species with large potential energy, which require lower activation energy in both electron impact reactions and heavy particle reactions. The high specific power deposition and contributions to gas heating from Franck–Condon processes produces high gas temperatures, which enable endothermic heavy particle reactions to occur. Endothermic reactions have a positive change in enthalpy ($\Delta H > 0$) whereas exothermic reactions have a negative change in enthalpy ($\Delta H < 0$).

With the addition of O_2 to NF_3, reactions between NF_x and O_x directly lead to the formation of FO through

$$NF_3 + O(^1D) \rightarrow NF_2 + FO, \quad \Delta H = -1.6\,eV, \tag{1a}$$

$$NF_2 + O \rightarrow NF + FO, \quad \Delta H = 0.7\,eV, \tag{1b}$$

$$F_2 + O \rightarrow F + FO, \quad \Delta H = -0.7\,eV, \tag{1c}$$

$$F + O_3 \rightarrow FO + O_2, \quad \Delta H = -1.2\,eV. \tag{1d}$$

The formation of NO occurs through endothermic reactions

$$N_2 + O \rightarrow N + NO, \quad \Delta H = 3.2\,eV, \tag{2a}$$

$$N_2 + O_2 \rightarrow NO + NO, \quad \Delta H = 1.8\,eV, \tag{2b}$$

and through exothermic reactions

$$N + O_2 \rightarrow NO + O, \quad \Delta H = -1.4\,eV, \tag{2c}$$

$$N + O_3 \rightarrow NO + O_2, \quad \Delta H = -5.5\,eV. \tag{2d}$$

The formation of N_2O dominantly occurs through the endothermic reaction

$$N_2 + O_2 \rightarrow O + N_2O, \quad \Delta H = 3.5\,eV. \tag{3}$$

FNO is largely produced by the exothermic reaction

$$NF_2 + O \rightarrow F + FNO, \quad \Delta H = -2.9\,eV. \tag{4}$$

These species produced in primary reactions lead to secondary reactions which form, for example, NO_2, through exothermic reactions

$$FNO + O \rightarrow F + NO_2, \quad \Delta H = -0.8\,eV, \tag{5a}$$

$$FO + NO \rightarrow F + NO_2, \quad \Delta H = -0.9\,eV, \tag{5b}$$

$$N_2O + NO \rightarrow N_2 + NO_2, \quad \Delta H = -1.5\,eV, \tag{5c}$$

$$NO + O_3 \rightarrow O_2 + NO_2, \quad \Delta H = -2.1\,eV, \tag{5d}$$

and the endothermic reaction

$$NO + O_2(a^1\Delta_g) \rightarrow O + NO_2, \quad \Delta H = 1.0\,eV. \tag{5e}$$

The full reaction pathway is fulfilled by reactions among NF_x species, O_x species and newly formed species (e.g., FO, NO, N_2O, NO_2, and FNO), which are either endothermic or exothermic.

In systems where the gas temperature approaches and exceeds 1000 K (0.1 eV), many of these endothermic reactions have appreciable rate coefficients, and so radical generation also occurs by heavy particle reactions in addition to electron impact. This is particularly important downstream of the plasma zone. For example, in addition to the primary reactions between NF_x and O_x, the formation of N_2O also occurs through the endothermic reaction

$$NO + NO \rightarrow O + N_2O, \quad \Delta H = 1.7\,eV \tag{6a}$$

and the exothermic reaction

$$N + NO_2 \rightarrow O + N_2O, \quad \Delta H = -1.7\,eV. \tag{6b}$$

The formation of NO also occurs through exothermic reactions

$$N + NO_2 \rightarrow NO + NO, \quad \Delta H = -3.4\,eV, \tag{7a}$$

$$NO_2 + O \rightarrow O_2 + NO, \quad \Delta H = -2.0\,eV, \tag{7b}$$

$$N_2O + O \rightarrow NO + NO, \quad \Delta H = -1.7\,eV. \tag{7c}$$

These reactions are not inhibited by the decrease in gas temperature as the gas flows downstream and results in NO being the dominant radical in the downstream region. In addition to reaction in Eq. (4), the formation of FNO also occurs through exothermic reactions

$$NF_2 + NO_2 \rightarrow FNO + FNO, \quad \Delta H = -2.1\,eV, \tag{8a}$$

$$NF_2 + FO \rightarrow FNO + F + F, \quad \Delta H = -0.6\,eV, \tag{8b}$$

$$F_2 + NO \rightarrow FNO + F, \quad \Delta H = -0.8\,eV. \tag{8c}$$

Even though these reactions are not inhibited by the decrease in gas temperature in the downstream, the FNO density does not increase since the consumption of FNO by O atoms [Eq. (5a)] offsets their contributions.

There is certainly a need and desire for reduced reaction mechanisms which would not only be computationally more expedient in multidimensional models, but also might lead to more intuitive interpretation of the results. In this regard, we performed sensitivity studies beginning with the complete reaction mechanism while excluding certain species and reactions. For example, we found that removing N_2O, FO, and O_3 (and their reactions) for our base case operating conditions produced a change in the densities of major species of less than 3%. Although this reduction in scope of the reaction mechanism provides reasonably consistent results with the complete mechanism, the reduced reaction mechanism would give considerably less good results if the pressure was increased to the degree that three-body reactions became important. A similar conclusion would hold for temperature. A reduced reaction mechanism for low power operation in which the increase in gas temperature is nominal could be constructed by removing nearly all of the N_xO_y species. This reduced mechanism would be insufficient for high power operation where endothermic reactions are important.

IV. VALIDATION

To validate the reaction mechanism, results obtained by global and 2d models were compared with optical emission spectroscopy (OES) measurements. The experimental setup was a remote CCP source with a volume of 1110 cm^3 sustained in an $Ar/NF_3/O_2 = 5/10/100$ gas mixture at 400 mTorr with a flow rate of 1150 sccm. The total input power was varied from 90 to 3000 W. The relative density of neutrals was measured through OES using actinometry.[33] In actinometry, the density of a reactive species, such as F, relative to a nonreactive gas of known density, such as Ar, is obtained from the ratio of optical emission originating from excited states that have similar thresholds and rate coefficients for electron impact excitation. In this regard, optical emission intensities were recorded from F atoms at 704 nm ($3p^2P^o \rightarrow 3s^2P$) and from the reference actinometry species, Ar, at 750 nm ($4p'[1/2] \rightarrow 4s'[1/2]^o$). $F(3p^2P^o)$ is 14.8 eV above the ground state while the Ar(4p'[1/2]) is 13.5 eV above the ground state. The relative density of F atoms is given by

$$[F] = C_{Ar}^{F} \frac{I(F^*)}{I(Ar^*)}[Ar], \tag{9}$$

where $I(Ar^*)$ is the intensity of the Ar 750 nm emission line, $I(F^*)$ is the intensity of the F 704 nm emission line, and C_{Ar}^{F} is the actinometric coefficient which is in principle a function of discharge parameters (e.g., EED, pressure, gas temperature).[34,35] In order for Eq. (9) to be valid, the emitting states must be dominantly populated by electron-impact excitation from the ground state and should decay dominantly by photon emission. The excitation to the emitting states of F and the actinometric species, Ar, should have similar thresholds and similar magnitudes for cross sections. That is, their rate coefficient for excitation should be similar. These requirements cannot always be strictly satisfied; however, it may be possible for $I(F^*)/I(Ar^*)$ to be proportional to $[F]/[Ar]$ over some range of plasma conditions which are chosen to make the actinometric coefficient a constant. It is possible to compute the dependence of the actinometric coefficient on the electron temperature with different

types of EEDs (e.g., Maxwellian, bi-Maxwellian, and Druyvesteyn) as discussed in Ref. 36. Assuming that emission from both states results from electron impact excitation of the ground state and the corresponding excitation cross sections for F and Ar have similar energy dependence, the actinometric coefficient in Eq. (9) is assumed to be 1.

To model the RPS for validation, both the global model and the 2d model were utilized. Schematics of the RPS addressed by the plug flow mode of the global model and by the CCP operation of the 2d model are shown in Fig. 2. In the global model, total power deposition by electrons is specified for a tube 8.4 cm in diameter and 20 cm long. The afterglow then extends for another 15 cm. In the 2d model, the RPS was simulated in Cartesian coordinates and has length of 20 cm, a width of 8 cm, and a depth of 6.9 cm, values to better represent the experiment. The top electrode was powered and the bottom electrode was grounded as are other boundaries. The bounding dielectrics to the electrodes are alumina. The gas enters from the left boundary and exits through the right boundary.

In the model of the CCP, as in the experiment, the power deposition is apportioned between ion acceleration in the sheath and electron heating in the bulk plasma (including secondary electrons). From a practical perspective, only the power deposition into electrons produces excited states and ionization. The power into electrons specified in the global model was determined by performing simulations using the 2d model which explicitly calculates all forms of power deposition for the experimental conditions. The power dissipated into electrons from the 2d model was then used as the input power in the global model so that side-by-side comparisons can be made to the experiments. In the 2d model, total power deposition for any given case was obtained by adjusting the amplitude of the 10 MHz applied voltage. As the power increases from 90 to 3000 W, the power dissipated by electrons indicated by the 2d model increases from 58 to 388 W while the fractional power dissipated by electrons decreases from 64% to 13%. This scaling results from the increased applied voltage and sheath potentials favoring power deposition by ions relative to electrons.

The densities of F atoms measured by OES-actinometry and predicted by the global and the 2d models are shown in Fig. 3. In both the experiments and simulations, the relative density of F atoms increases with power until saturating at high power. The density of F atoms predicted by the model reaches its maximum at about 1200 W. As the power increases above 1200 W, the density of F atoms slightly decreases as the increase of the F density produced by additional dissociation of NF_3 is counterbalanced by the rarefaction of the gas by increased gas temperature. The density of F atoms predicted by the 2d model saturates at higher power compared with experiments and results from the global model; however, the differences are not large.

Other validation was made between results from the global model and OES measurements performed in a microwave plasma by Kastenmeier *et al.*[5] A plasma was sustained in an O_2/NF_3 mixture at 1 Torr with 1400 W power at 2.45 GHz, which was also the input power in the global model in plug flow mode. The NF_3 flow rate was 300 sccm for all cases. The densities of O, N_2, and NO predicted by the global model and measured by OES are in Fig. 4 as a function of the ratio of O_2 to NF_3 flow rate. The density of O atoms increases linearly with increasing flow rate of O_2 at low values, and beginning to saturate at high values due to the finite power deposition. The density of N_2 decreases in favor of the generation of NO. In the experiments, the density of NO remains almost constant for flow ratios of $O_2/NF_3 < 0.6$ and sharply increases when the ratio is above 0.6. In the global simulations, the density of NO also remains nearly constant for a ratio of O_2/NF_3 smaller than 0.6 but increases less abruptly than that in the experiments for larger ratios.

The formation of NO is mainly through the endothermic reactions in Eqs. (2a) and (2b) with an activation energy of several eV which favors high gas temperature. The depletion of NO is mainly through exothermic reactions in Eq. (8c) and

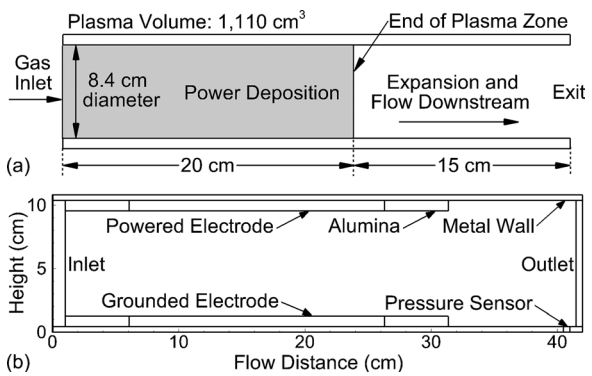

FIG. 2. Schematic of the remote plasma source addressed by (a) the plug flow mode of the global model and (b) the CCP operation of the 2d model. The gas is pumped in from the left and exits at the right side.

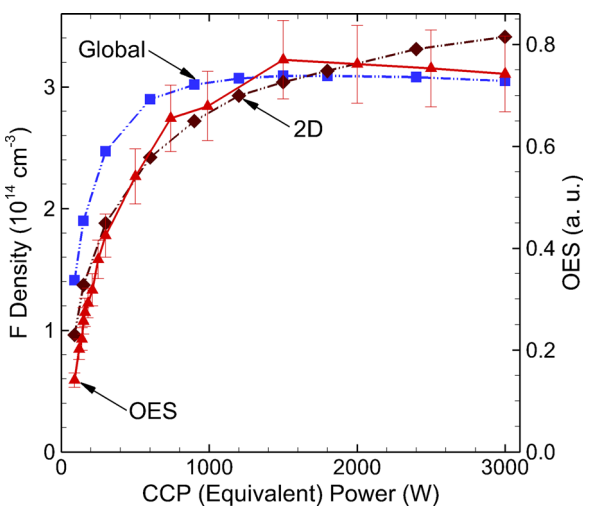

FIG. 3. (Color online) Comparison of the global simulation results (blue dotted lines), the 2d simulation results (brown dotted lines) and the OES measurements (red solid lines) for the densities of F atoms at the end of the plasma zone. Discharge conditions: $Ar/NF_3/O_2 = 5/10/100$, 400 mTorr, 1150 sccm, and CCP equivalent power: 90–3000 W (power into electrons: 58–388 W).

$$NO + NO \rightarrow N_2 + O_2, \quad \Delta H = -1.8\,eV, \tag{10a}$$

$$NO + N \rightarrow N_2 + O, \quad \Delta H = -3.2\,eV. \tag{10b}$$

NF_3 is almost fully dissociated for the given power. Adding O_2 contributes to more Franck–Condon heating, and so the gas temperature increases from 1840 to 2810 K as the flow rate of O_2 increases from 30 to 450 sccm, which benefits the formation of NO. The smaller slope obtained from the simulation when the ratio of O_2/NF_3 is larger than 0.6 may be due to underestimates of the gas temperature or the sensitivity of the density of N_2 molecules to the wall recombination coefficients.

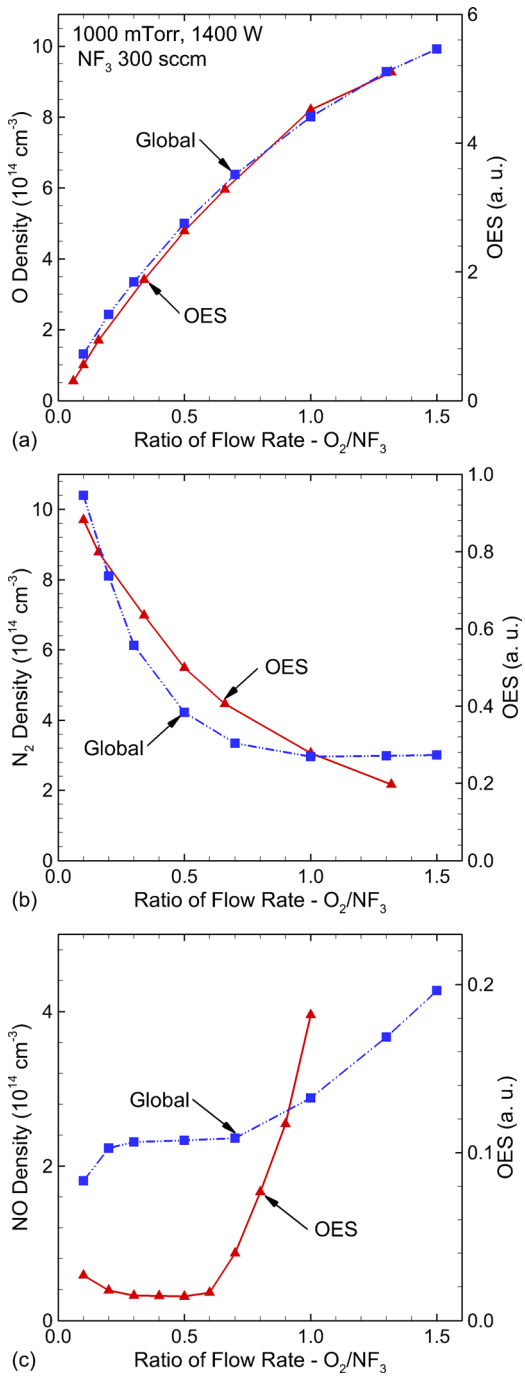

FIG. 4. (Color online) Comparison of the global simulation results (blue dotted lines) and the OES measurements (red solid lines) for the densities of (a) O atoms, (b) N_2 molecules, and (c) NO molecules at the end of the plasma zone. The OES measurements are for a microwave discharge conducted by Kastenmeier *et al.* (Ref. 5) Discharge conditions: ratio of flow rate for O_2/NF_3 = X, 1 Torr, (300 + 300X) sccm, X = 0–1.5, and microwave power (into electrons): 1400 W.

V. SCALING OF REMOTE PLASMA SOURCES BY PLUG FLOW MODELING

A schematic of the RPS addressed by the plug flow global model is shown in Fig. 2(a). The base case is an $Ar/NF_3/O_2 = 5/10/100$ gas mixture at 400 mTorr with a flow rate of 1150 sccm. The total input power to electrons is 237 W which corresponds to a total CCP power of 900 W. Densities of charged particles and neutrals as a function of flow distance are shown in Figs. 5 and 6. In the plasma zone, the discharge is highly electronegative with a ratio of negative ions to electrons of 25–70. The electron density increases during the flow to a maximum of $7.2 \times 10^9\,cm^{-3}$ while the electron temperature decreases from 4.0 to 3.5 eV. These trends result in part from the manner of specifying power. The power is specified to be uniform over the first 20 cm of the flow tube. The increase in electron density is due to the decrease in the mole fraction of molecular species and increase in the mole fraction of atomic species, the latter of which have a lower rate of specific power deposition than the molecular species. The electron density increases so as to maintain the desired uniform power deposition. The electron temperature decreases to reflect the less attaching nature of the more dissociated (and more atom dominated) gas mixture as the gas flows downstream. A lower electron temperature is enabled by there being less ionization required to balance the reduced rate of attachment. This decrease in T_e occurs in spite of the increase in gas temperature and slow decrease in gas density which then increases the rate of loss of charged species by ambipolar diffusion.

The dominant positive ions in the plasma zone are O_2^+ and NO^+. With the dissociation of O_2 and the formation of

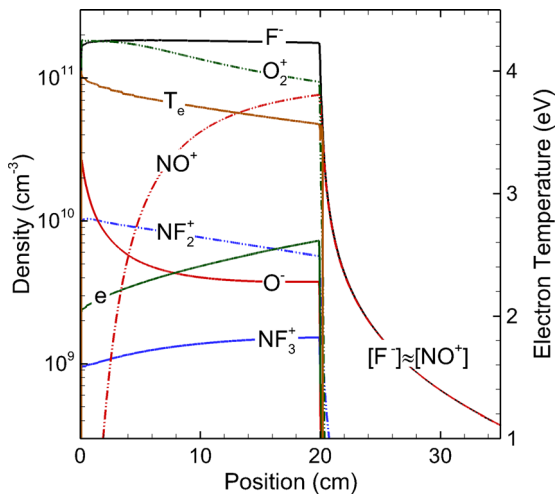

FIG. 5. (Color online) Densities of charged particles and electron temperature in the plug flow mode of the global model. Discharge conditions: $Ar/NF_3/O_2$ = 5/10/100, 400 mTorr, 1150 sccm, and CCP equivalent power: 900 W (power into electrons: 237 W).

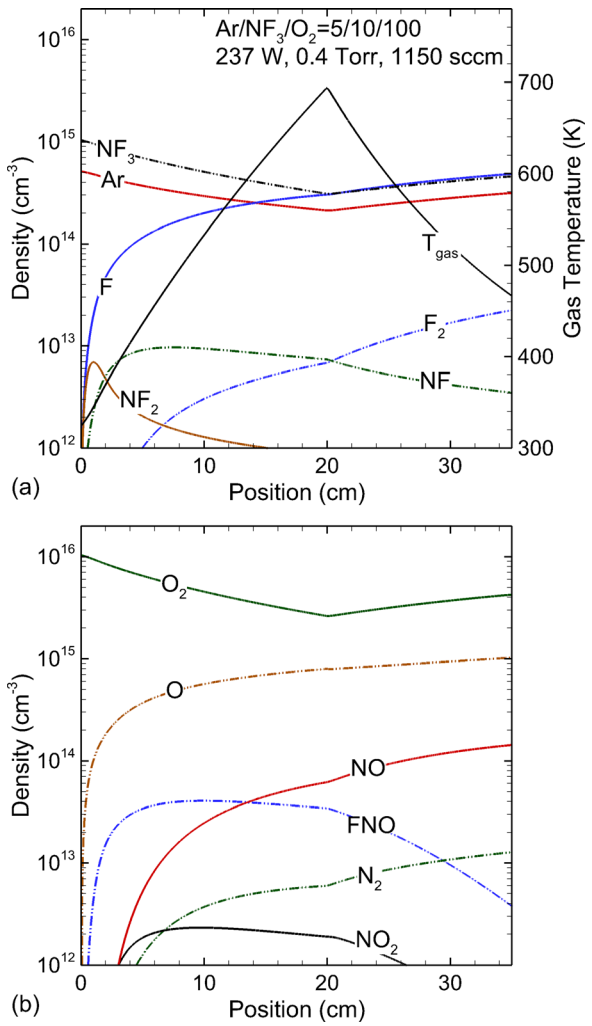

FIG. 6. (Color online) Densities of the neutrals and gas temperature in the plug flow mode of the global model. Discharge conditions: $Ar/NF_3/O_2 = 5/10/100$, 400 mTorr, 1150 sccm, and CCP equivalent power: 900 W (power into electrons: 237 W).

NO, the density of O_2^+ decreases from 1.8 to $0.9 \times 10^{11}\,cm^{-3}$ while the density of NO^+ increases up to $7.6 \times 10^{10}\,cm^{-3}$. Although the ionization potential of NO (9.3 eV) is lower than O_2 (12.1 eV), and charge exchange to NO from all positive ions is exothermic, the significant difference in the density of parent molecules results in higher density of O_2^+ than NO^+ by ≈20%. The formation of negative ions is largely due to dissociative attachment of NF_x (x = 1–3) by thermal electrons

$$e + NF_x \rightarrow NF_{x-1} + F^- \tag{11}$$

and dissociative attachment of O_2 by nonthermal electrons

$$e + O_2 \rightarrow O + O^-. \tag{12}$$

There is essentially no energy threshold for dissociative electron attachment to NF_x, and so attachment rapidly occurs with thermal electrons (that is, electrons having a low, near ambient, temperature). On the other hand, electron dissociative attachment with O_2 has a threshold energy of 3.6 eV, which is the potential energy difference between $O + O^-$ and the ground state O_2. As a result, there is production of both O^- and F^- in the plasma zone, but only production of F^- downstream where T_e rapidly decays to thermal values. In the downstream region, the plasma rapidly transitions to an ion–ion plasma (within a cm of the end of the plasma zone) composed dominantly of F^- and NO^+. There is essentially no electron impact ionization downstream of the plasma zone; however, there is production and mixing of positive ions, through Penning processes and charge exchange. As the ionization potential of NO (9.3 eV) is the lowest among the major positive ions, charge exchange and Penning ionization predominantly favor the formation of NO^+ ions. The end result is that charge neutrality downstream is maintained by $[F^-] \approx [NO^+]$. Since the mobilities of F^- and NO^+ are commensurate, there is little ambipolar enhancement of the rates of diffusion of the ions. The steady decay of the densities of F^- and NO^+ in the downstream region predominantly results from ion–ion neutralization. The loss of ions by simple thermal diffusion accounts for less than 1% of the total loss.

The densities of neutrals and gas temperature T_g for the base case are shown in Fig. 6. In the plasma zone, NF_3 is rapidly depleted through electron dissociative attachment, $e + NF_3 \rightarrow NF_2 + F^-$, and dissociative excitation, $e + NF_3 \rightarrow NF_2 + F + e$. The densities of F and NF_2 sharply increase to $6 \times 10^{12}\,cm^{-3}$ with approximately the same rate within 1 cm of the gas inlet. Further downstream, the density of NF_2 decreases while the densities of NF and FNO increase as NF_2 is decomposed to NF through electron impact dissociative attachment, $e + NF_2 \rightarrow NF + F^-$ and dissociative excitation, $e + NF_2 \rightarrow NF + F + e$. At this point, there is a sufficient density of dissociation fragments that mutual reactions add to the dissociation rate. For example, in addition to the reaction of $NF_2 + O$ producing FO [Eq. (1b)] and FNO [Eq. (4)], NF_2 is depleted by reactions with N atoms

$$NF_2 + N \rightarrow NF + NF, \quad \Delta H = -0.1\,eV. \tag{13}$$

Although the dominant trend is dissociation and fragmentation, there are bimolecular reactions that convert NF_2 back to NF_3

$$NF_2 + F_2 \rightarrow F + NF_3, \quad \Delta H = -1.0\,eV, \tag{14a}$$

$$NF_2 + NF_2 \rightarrow NF + NF_3, \quad \Delta H = 0.4\,eV. \tag{14b}$$

As bimolecular recombination to reform NF_3 requires NF_2 and F_2 (the pressure is too low for three-body processes to be important) adding O_2 which rapidly consumes NF_2 [Eqs. (1b) and 4] maintains the fractional dissociation of NF_3 and increases the density of F. This trend is consistent with the results of experiments where adding O_2 to NF_3 during etching of Si and SiO_2 generally increases rates of surface reactions requiring F atoms.[37]

NF dissociates to form N and F through electron impact dissociative excitation and attachment. NF can assist in the decomposition of NF_3 and reform NF_2 by

$$NF_3 + NF \rightarrow NF_2 + NF_2, \quad \Delta H = -0.4\,eV. \tag{15}$$

Another channel for the consumption of NF is through mutual reactions to form N_2 and F_2

$$NF + NF \rightarrow N_2 + F + F, \quad \Delta H = -3.6\,eV, \tag{16a}$$

$$NF + NF \rightarrow N_2 + F_2, \quad \Delta H = -5.2\,eV. \tag{16b}$$

Although these reactions are both exothermic, the reaction in Eq. (16a) has an activation energy of 1250 K and so contributes less to the formation of N_2 and F_2 and the depletion of NF at temperatures significantly below 1000 K. The F_2 formed by the mutual reaction of NF is itself rapidly dissociated in the plasma by dissociative attachment. In comparison, N_2 is relatively stable.

NO is dominantly generated by reactions of N_2 with O and O_2 [Eqs. (2a) and (2b)] while the source of N_2 is mainly through the mutual reactions of NF [Eqs. (16a) and (16b)] and surface recombination. The contribution of reactions of N atoms with O_2 and O_3 [Eqs. (2c) and (2d)] to the formation of NO is small as the density of N atoms ($\sim 10^{10}\,cm^{-3}$) is smaller than N_2 ($\sim 10^{12}\,cm^{-3}$) by 2 orders of magnitudes. The density of NO is highly dependent on the fragmentation of NF_3 to form NF which is the dominant gas phase precursor to N_2. The recombination probability of N at surfaces (assumed to be 0.01), not extensively investigated here, also impacts the inventory of N_2.

At the end of the plasma zone, F and O are the dominant dissociation products with densities of $3 \times 10^{14}\,cm^{-3}$ and $8 \times 10^{14}\,cm^{-3}$, respectively. NO is the dominant molecular reaction product, with a density of $6 \times 10^{13}\,cm^{-3}$, produced by endothermic reactions facilitated by an increase in T_g to $\approx$700 K at the end of the plasma zone. This increase in T_g is mainly sustained by dissociative excitation and attachment which produces high-energy neutrals through the Franck–Condon effect. Being an atomic species which is not chemically depleted, the density of Ar indicates the heating, rarefaction, expansion, and cooling of the gas. The decrease of Ar density in the plasma zone is due to gas heating and also due to the dissociation of the molecular feedstock gases which, for constant pressure, expands the gas and increases flow rate. Downstream of the plasma zone, T_g rapidly decreases to 470 K due to thermal conduction to the walls, resulting in contraction of the gas and a rebound in densities of Ar, NF_3, F, and NO.

The decrease in T_g and rebound in densities is likely overestimated in the global model which does not account for diffusive axial transport or axial thermal conduction. The walls of the flowtube are also held at 325 K, which likely speeds the rate of thermal condition. In spite of the gas-temperature initiated rebound in densities, the density of NF decreases from 7.4 to $3.5 \times 10^{12}\,cm^{-3}$ downstream due to its depletion through mutual, exothermic reactions [Eqs. (16a) and (16b)]. From the perspective of relative rates of reaction, the formation of NF is an endothermic process whereas the depletion of NF is an exothermic process. The decrease in gas temperature (and electron temperature, discussed below) downstream favors depletion of NF.

A. Power deposition

The densities of neutrals at the end of plasma zone and at the exit of the flow tube are shown in Figs. 7 and 8 as a function of CCP equivalent power of 90–3000 W. As the densities of charged species and excited states are negligible compared with the densities of neutrals, the fractional dissociation of NF_3 can be approximated by

$$f_{NF_3} = \left(1 - \frac{[Ar]_0}{[Ar]}\frac{[NF_3]}{[NF_3]_0}\right) \times 100\%, \tag{17}$$

where, for example, $[Ar]_0$ is the density at the inlet. The fractional dissociation of NF_3 at the end of the plasma zone increases from 7% to 43% as the power increases from 90 to 3000 W and the density of F atoms increases from $1.4 \times 10^{14}\,cm^{-3}$ to saturate at $3.1 \times 10^{14}\,cm^{-3}$. In the plasma zone, the F atoms are created through three channels—dissociative attachment of NF_x by thermal electrons followed by neutralization of F^-, dissociative excitation of NF_x, and heavy particle collisions with F atoms as products. These

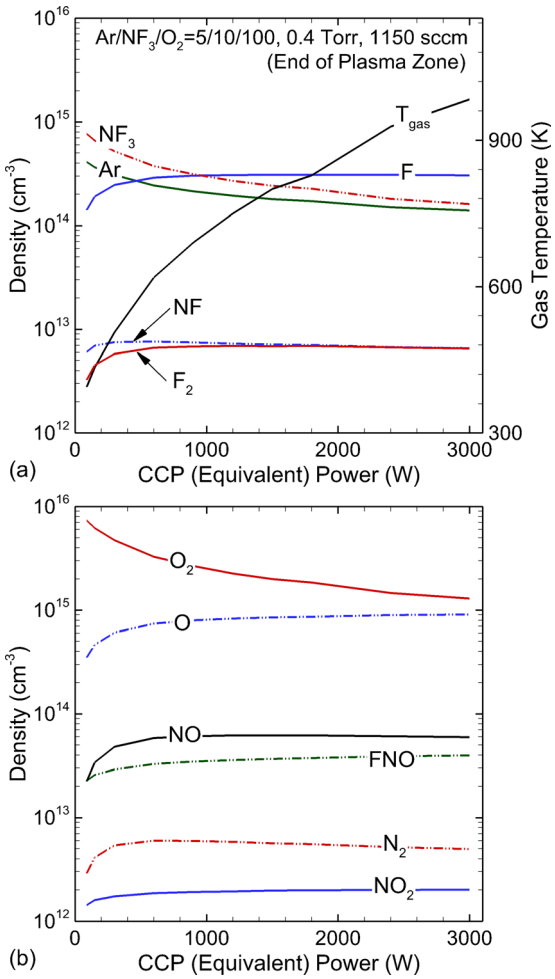

FIG. 7. (Color online) Densities of neutrals and gas temperature at the end of the plasma zone in the plug flow mode of the global model. Discharge conditions: $Ar/NF_3/O_2 = 5/10/100$, 400 mTorr, 1150 sccm, and CCP equivalent power: 900 W (power into electrons: 237 W).

latter reactions include the exothermic processes in Eqs. (4), (5a), (5b), (16a), and

$$NF_2 + N \rightarrow N_2 + F + F, \quad \Delta H = -3.7\,eV, \tag{18a}$$

$$NF + N \rightarrow N_2 + F, \quad \Delta H = -6.7\,eV. \tag{18b}$$

The F atoms are mainly consumed through wall recombination to form F_2 and endothermic reactions with FO

$$F + FO \rightarrow O + F_2, \quad \Delta H = 0.7\,eV. \tag{19}$$

As the power increases from 90 to 3000 W, the T_g increases almost linearly from 395 to 985 K with increasing fractional dissociation of NF_3 reflecting the dominant role in gas heating due to the Franck–Condon effect. The density of F atoms does not monotonically increase. Rather, the density of F saturates at $3.1 \times 10^{14}\,cm^{-3}$ despite of the increasing fractional dissociation of NF_3. A portion of that saturation results from the rarefaction resulting from gas heating. A similar trend holds for the density of NO, whose rate of formation based on endothermic processes [Eqs. (2a)and (2b)] increases with increasing gas temperature while being offset by the rarefaction of the gas with gas heating.

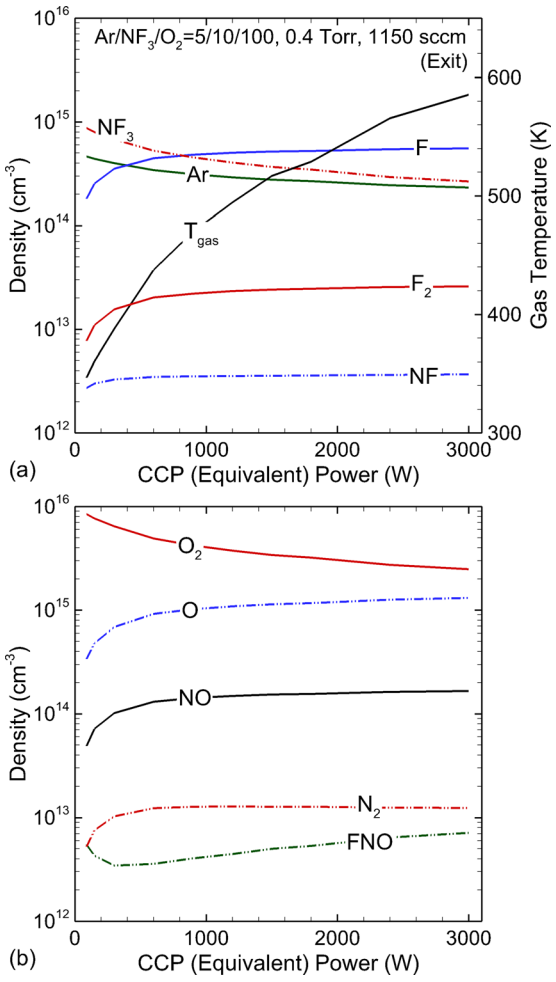

FIG. 8. (Color online) Densities of neutrals and gas temperature at exit in the plug flow mode of the global model. Discharge conditions: $Ar/NF_3/O_2 = 5/10/100$, 400 mTorr, 1150 sccm, and CCP equivalent power: 900 W (power into electrons: 237 W).

The trends for neutral densities at the exit of the tube as a function of power (shown in Fig. 8) are similar to those at the end of plasma zone. The densities of most neutrals (e.g., Ar, NF_3, F, O, and NO) at the exit are larger than at the end of plasma zone simply because of cooling of the gas. However, the densities of NF, FNO, and NO_2 are smaller than those at the end of the plasma zone due to consumption of these species through exothermic mutual reactions and reactions with O atoms [Eqs. (5a), (7b), and (16a), (16b)]. Since these reactions are exothermic, they are not inhibited by the decrease in T_g as for endothermic reactions. The fractional dissociation of NF_3 continues to increase to the exit as exothermic reactions with metastable species such as $O(^1D)$ [Eq. (1a)] and NF [Eq. (15)] continue consuming NF_3.

B. NF_3 flow rate

Plasma properties were investigated for NF_3 flow rates from 50 to 500 sccm while maintaining 300 W into electrons, or an equivalent CCP power of ≈1600 W. The other discharge parameters are the same as the base case (400 mTorr, 50 sccm Ar, and 1000 sccm O_2). The resulting densities of neutrals at the end of the plasma zone and at the exit of the flow tube are shown in Figs. 9 and 10. With constant power and with increasing NF_3 flow rate, the fractional dissociation of NF_3 decreases from 41% (50 sccm) to 22% (500 sccm). With the average density of NF_3 increasing with flow rate, the density of F increases and saturates at $5 \times 10^{14}\,cm^{-3}$ at a high flow rate. The saturation of the F density while the density of NF_3 continues to increase indicates that radical production is power-limited although a portion of this saturation is due to rarefaction. With increasing flowrate of NF_3, T_e in the plasma zone increases from 3.2 to 4.5 eV to provide the additional ionization required to compensate the higher rate of attachment to NF_3.

The density of O_2 moderately decreases from 2.0 to $1.3 \times 10^{15}\,cm^{-3}$, a consequence of the decrease in O_2 mole fraction, as the NF_3 flow rate increases while keeping pressure constant. The density of O significantly decreases from 1.2×10^{15} to $1.6 \times 10^{14}\,cm^{-3}$ due to the larger fraction of the discharge power that is dissipated by NF_3, and the higher rate of reaction of O with NF_x radicals. The density of NO decreases from 5.1 to $2.4 \times 10^{13}\,cm^{-3}$ due to the decrease in density of O and the more rapid consumption of NO through reaction with F_2 [Eq. (8c)]. The latter reaction produces the increasing density of FNO, from 1.8×10^{13} to $1.3 \times 10^{14}\,cm^{-3}$.

T_g monotonically increases from 760 to 1050 K at the end of the plasma zone and from 460 to 800 K at the exit for the increase in NF_3 flow rate of 50–500 sccm. The higher rate of dissociative attachment and excitation of NF_x with increasing flow rate produces significant Franck–Condon heating.

VI. REMOTE PLASMA SOURCE SUSTAINED IN CAPACITIVELY COUPLED PLASMA

Although global modeling is quite valuable for system studies and developing reaction mechanisms, geometrical

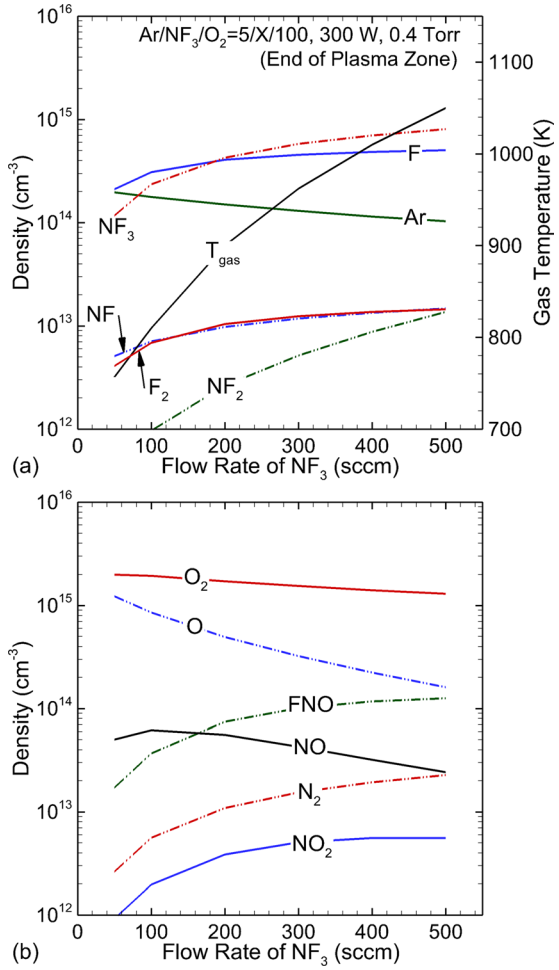

FIG. 9. (Color online) Densities of neutrals and gas temperature at the end of the plasma in the plug flow mode of the global model. Discharge conditions: $Ar/NF_3/O_2$ = 5/X/100, 400 mTorr, (1050 + 10X) sccm, X = 5–50, and power into electrons: 300 W.

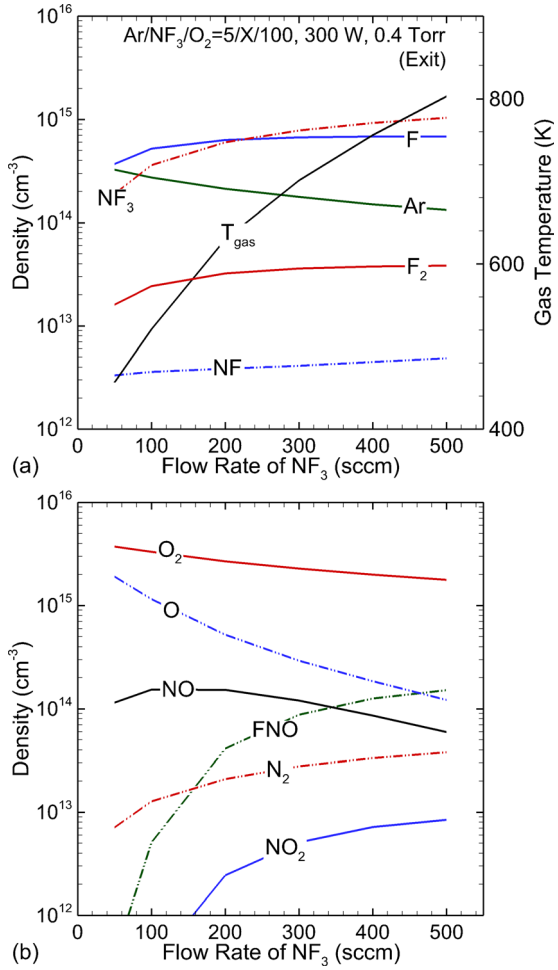

FIG. 10. (Color online) Densities of neutrals and gas temperature at exit in the plug flow mode of the global model. Discharge conditions: $Ar/NF_3/O_2$ = 5/X/100, 400 mTorr, (1050 + 10X) sccm, X = 5–50, and power into electrons: 300 W.

and transport dependent processes are difficult to accurately represent. With the goal of investigating the consequences on radical generation of system specific parameters, the RPS was simulated with the 2d model using the geometry schematically shown in Fig. 2 and described in Sec. II. The secondary electron emission coefficient for ions was 0.15 on the electrodes, 0.05 on the dielectric, and 0.02 on the metal walls. The base case conditions are the same as for the global model—$Ar/NF_3/O_2 = 5/10/100$ at 400 mTorr and a flow rate of 1150 sccm. The voltage on the powered electrode was adjusted to 1050 V at 10 MHz to sustain the CCP with a total power deposition of 900 W. The self dc bias on the powered electrode is −293 V.

In addition to investigating the scaling of radical production in RPS systems, the following results serve as a case study for the extreme sensitivity of CCPs sustained in moderate pressure, highly attaching gas mixtures to reactor design parameters. The origin of this sensitivity is the very rapid transition between net attachment and net ionization as a function of electron temperature. For example, EEDs were generated by solving Boltzmann's equation for the initial gas mixture ($Ar/NF_3/O_2 = 5/10/100$, 400 mTorr) for a range of E/N. The net ionization coefficient, $\alpha' = \alpha - \beta$ (cm^{-1}) was computed, where α is the first Townsend coefficient for ionization and β is the second Townsend coefficient for attachment. Both α and β are sensitive functions of E/N, with α steeply increasing with increasing E/N and β steeply decreasing with E/N. α' changes from $-0.05\,cm^{-1}$ (net attachment) to $+0.05\,cm^{-1}$ (net ionization) over a range of T_e of only 0.4 eV, or a fractional change in E/N of only 15%. In CCPs where electric fields can vary by an order of magnitude over a small fraction of the interelectrode distance, this sensitivity can result in significant changes in plasma properties.

Time averaged densities of electrons, T_e, ionization source by bulk electrons S_b and ionization by secondary electrons emitted from electrodes, S_s, are shown in Fig. 11 for the base case. The electric field is naturally enhanced at the edge of the electrodes at the intersection with the alumina insulators, a triple point—additional enhancement is produced in the sheath. This electric field enhancement locally heats electrons and increases electron power deposition, which increases the local rate of ionization. This local enhancement produces a local maximum of $1.8 \times 10^{10}\,cm^{-3}$

in electron density, whereas the electron density in the bulk plasma is $4 \times 10^9\,\mathrm{cm}^{-3}$. This sharp gradient in plasma properties is in part enabled by the extreme sensitivity of α' to small changes in T_e and E/N.

Secondary electrons play an important role in CCPs sustained in electronegative gas due to their contribution to net ionization. S_s is quite uniform and high ($2 \times 10^{16}\,\mathrm{cm}^{-3}\,\mathrm{s}^{-1}$) near the surface of the powered electrode whereas the net ionization by bulk electrons S_b is negative (meaning net loss by attachment and recombination) in most of the RPS region except the region near the edge of the powered electrode. The RPS is then sustained by ionization by secondary electrons.

In our investigation of RPS using the global model, the power deposited into electrons obtained from the 2d model was used as input power. The electron density in the middle of the reactor from the global model is also about $4–5 \times 10^9\,\mathrm{cm}^{-3}$, similar to that for the 2d model. However, T_e in the global model, 3.8 eV, is significantly higher than predicted by the 2d model in the bulk plasma, 2.6 eV. The lower T_e in the 2d model for similar electron densities is enabled by the more efficient contributions to ionization by the secondary electrons. With there being only bulk electrons in the global model, a higher T_e is required to sustain the plasma. With axial transport and no barriers placed downstream, such as grids, the CCP is not confined in the source region. The effective plasma volume exceeds that strictly defined by the electrodes. The plasma extends downstream beyond the electrodes to the pump-port with a density of $1.6 \times 10^9\,\mathrm{cm}^{-3}$, and an electron temperature of about 3 eV. The specific power deposition ($\mathrm{W/cm}^3$) is therefore smaller.

The densities of F^-, O_2^+, and NO^+ are shown in Fig. 12 for the CCP source. Similar to the global model, the density of F^- in the plasma zone is $\approx 2 \times 10^{11}\,\mathrm{cm}^{-3}$, producing an electronegativity of about 50. (Electronegativity is the ratio of the density of all negative ions to the density of electrons ($[M^-]/[e]$.) As the plasma flows downstream, there is a transition into a nearly ion-ion plasma in which charge neutrality is maintained by $[F^-] \approx [NO^+] + [O_2^+]$. NO^+ is the dominant positive ion with a density of $7 \times 10^{10}\,\mathrm{cm}^{-3}$ at the exit followed by O_2^+ with a density of $2 \times 10^{10}\,\mathrm{cm}^{-3}$. The significant amount of O_2^+ is due to ionization which occurs downstream due to axial transport of electrons and thermal conductivity, an effect that is not captured in the global model where the downstream positive ion density is essentially all NO^+. Since expansion of the plasma downstream is nearly unavoidable at the pressures of interest, RPS must employ distance or grids to confine the charged particle fluxes, and so enable purely neutral driven etching downstream.

The time averaged densities of neutrals shown in Figs. 13 and 14 have similar dependencies on flow distance as predicted by the global model. NF_3 and O_2 dissociate and undergo rarefaction as they flow between the electrodes and are heated. The dominant radicals at the end of the plasma zone are F, O and NO, with densities of 2.7, 4.3, and $0.7 \times 10^{14}\,\mathrm{cm}^{-3}$. The major gas heating mechanism in the

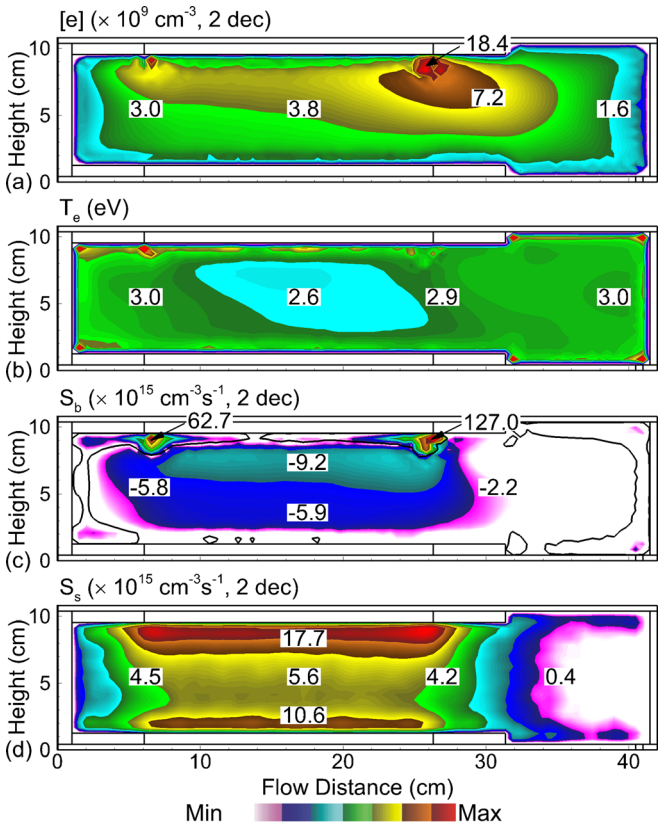

FIG. 11. (Color online) Time averaged (a) electron density, (b) electron temperature, electron ionization source by (c) bulk electrons and (d) secondary electrons in a remote plasma source driven by capacitively coupled power. Discharge conditions: $Ar/NF_3/O_2$ = 5/10/100, 400 mTorr, 1150 sccm, 900 W, and 10 MHz.

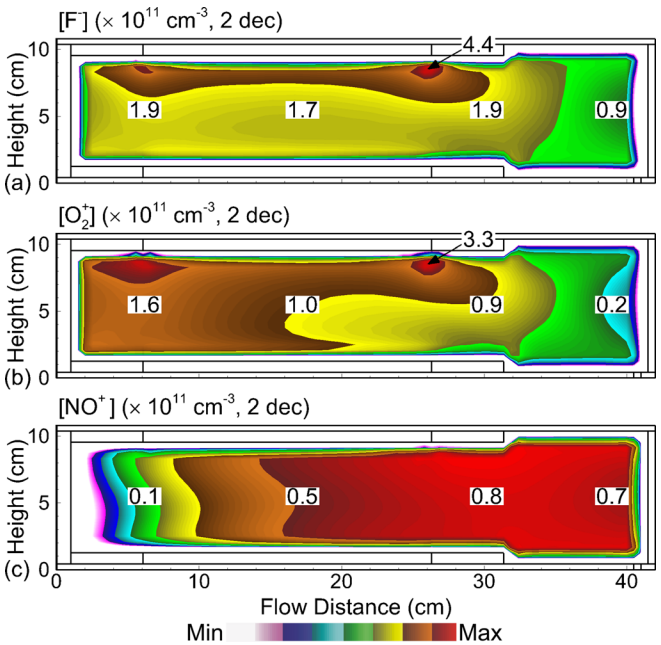

FIG. 12. (Color online) Time averaged densities of (a) F^-, (b) O_2^+, and (c) NO^+ ions in a remote plasma source driven by capacitively coupled power. Discharge conditions: $Ar/NF_3/O_2 = 5/10/100$, 400 mTorr, 1150 sccm, 900 W, and 10 MHz.

plasma zone is Franck–Condon heating following electron impact dissociation of molecular species. The gas temperature, shown in Fig. 14(f), increases from room temperature at the inlet to 670 K at the end of the plasma zone, which is accompanied by the increasing density of the dissociation products, F and O. The density of NO increases to $7 \times 10^{13}\,\mathrm{cm}^{-3}$ at the end of the plasma zone as the gas temperature increases. Recall that NO is predominantly produced through the endothermic reactions in Eqs. (2a) and (2b).

As NF_3 flows into the reactor, it is rapidly dissociated to NF_2, which in turn is dissociated to NF. The density of NF_3 monotonically decreases from 1 to $0.3 \times 10^{15}\,\mathrm{cm}^{-3}$ flowing through the plasma zone, whereas the density of NF_2 has a momentary maximum of $4.4 \times 10^{12}\,\mathrm{cm}^{-3}$, a result of its production by dissociation of NF_3 and its depletion by its own dissociation. The densities of NF_x are asymmetric across the height of the reactor. The densities of NF_3 and NF_2 are lower and the density of NF higher near the upper powered electrode, a consequence of the higher power deposition at the edge of the sheath of the powered electrode. The F density monotonically increases 0 to $3.4 \times 10^{14}\,\mathrm{cm}^{-3}$ with axial flow distance—first due to the integral production by dissociation of NF_x. The increase in density far downstream is in part a consequence of the gas cooling.

The same general trends hold for O_2 and O—a monotonic decrease in the density of O_2 from 1 to $0.3 \times 10^{16}\,\mathrm{cm}^{-3}$, more highly dissociated near the powered electrode, and a monotonic increase in O atom density to $4.9 \times 10^{14}\,\mathrm{cm}^{-3}$ with flow distance. The increasing densities of O and N_2, coupled with the increase in gas temperature, result in a monotonic increase in the density of NO with flow distance. The density of N atoms also monotonically increases with flow distance, but its contribution to the creation of NO is negligible as the N density ($\approx 10^{10}\,\mathrm{cm}^{-3}$) is 2 orders of magnitude smaller than N_2 density ($\approx 10^{12}\,\mathrm{cm}^{-3}$).

The densities of FNO and NO_2 are less sensitive to flow and gas temperature, with densities in the gap which reflect the source of their precursors by electron impact. For

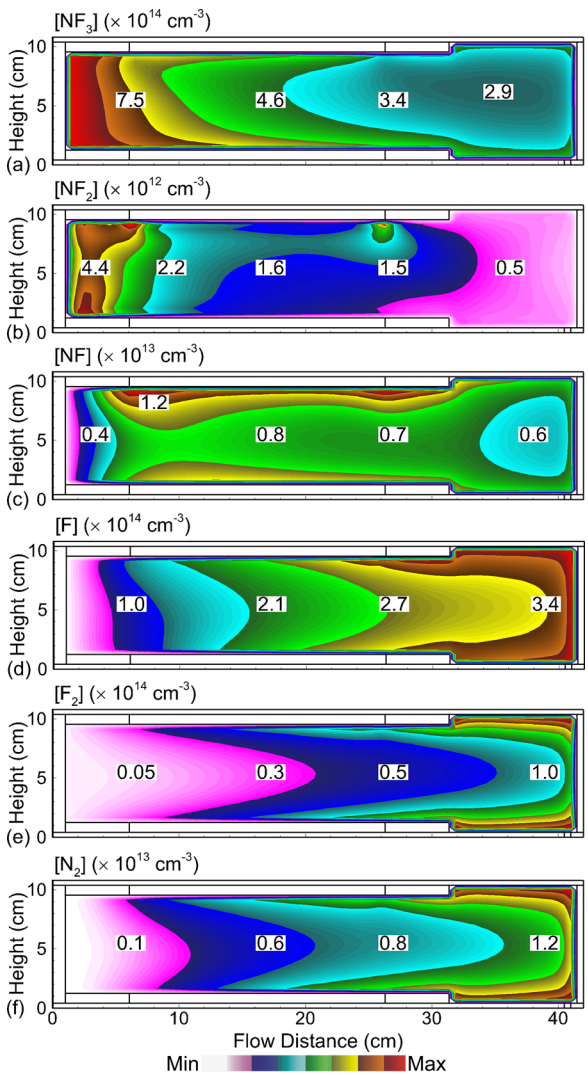

FIG. 13. (Color online) Time averaged densities of (a) NF_3, (b) NF_2, (c) NF, (d) F, (e) F_2, and (f) N_2 in a remote plasma source driven by capacitively coupled power. Discharge conditions: $Ar/NF_3/O_2 = 5/10/100$, 400 mTorr, 1150 sccm, 900 W, and 10 MHz.

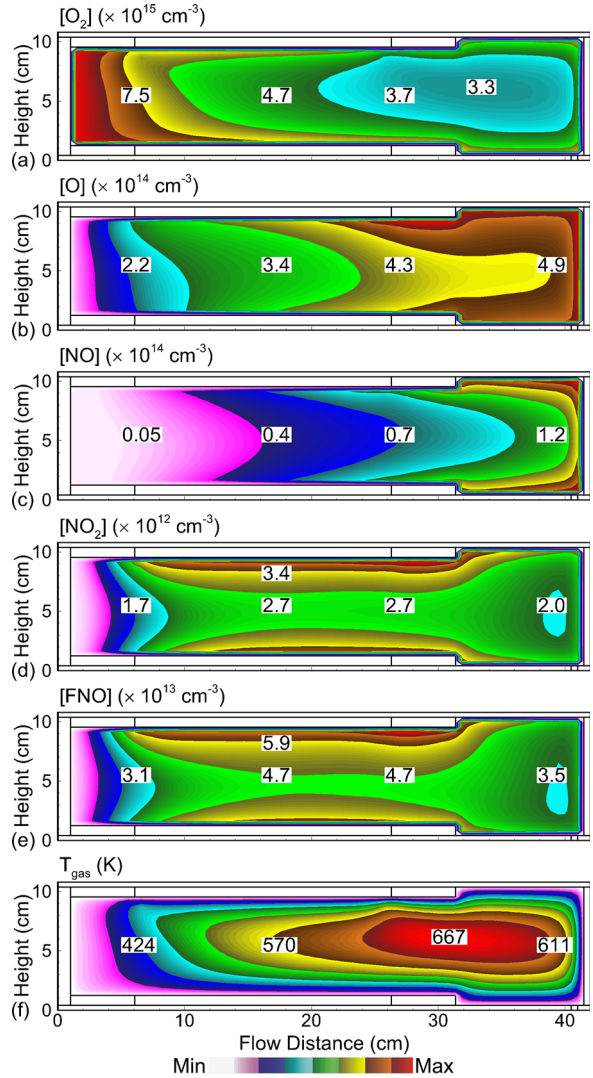

FIG. 14. (Color online) Time averaged densities of (a) O_2, (b) O, (c) NO, (d) NO_2, (e) FNO, and (f) the gas temperature in a remote plasma source driven by capacitively coupled power. Discharge conditions: $Ar/NF_3/O_2 = 5/10/100$, 400 mTorr, 1150 sccm, 900 W, and 10 MHz.

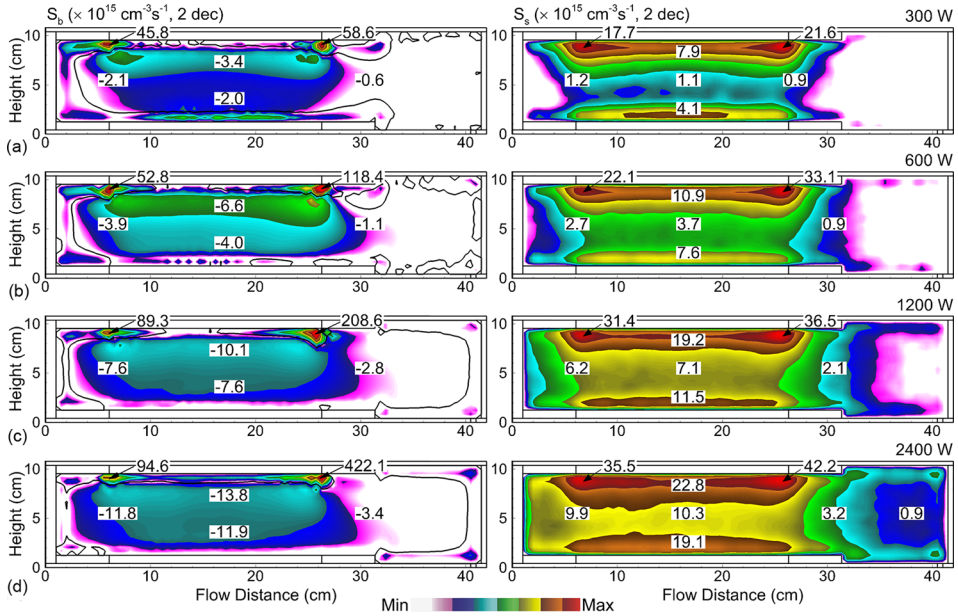

FIG. 15. (Color online) Time averaged electron ionization source by bulk electrons and secondary electrons in a remote plasma source driven by capacitively coupled power of (a) 300 W, (b) 600 W, (c) 1200 W, and (d) 2400 W. Discharge conditions: $Ar/NF_3/O_2 = 5/10/100$, 400 mTorr, 1150 sccm, 300–2400 W, and 10 MHz.

example, the density of FNO increases from $4.7 \times 10^{13}\,cm^{-3}$ at the center of the gap to $5.9 \times 10^{13}\,cm^{-3}$ at the surface of the powered electrode, similar to the increase in NO_2 density from 2.7 to $3.4 \times 10^{12}\,cm^{-3}$. This increase is in part due to the lower gas temperature at the electrodes due to thermal conduction. However, the formation of FNO and NO_2 occurs through exothermic reactions [Eqs. (4), (5a)–(5d), and (8)], which are not inhibited by this decrease in gas temperature.

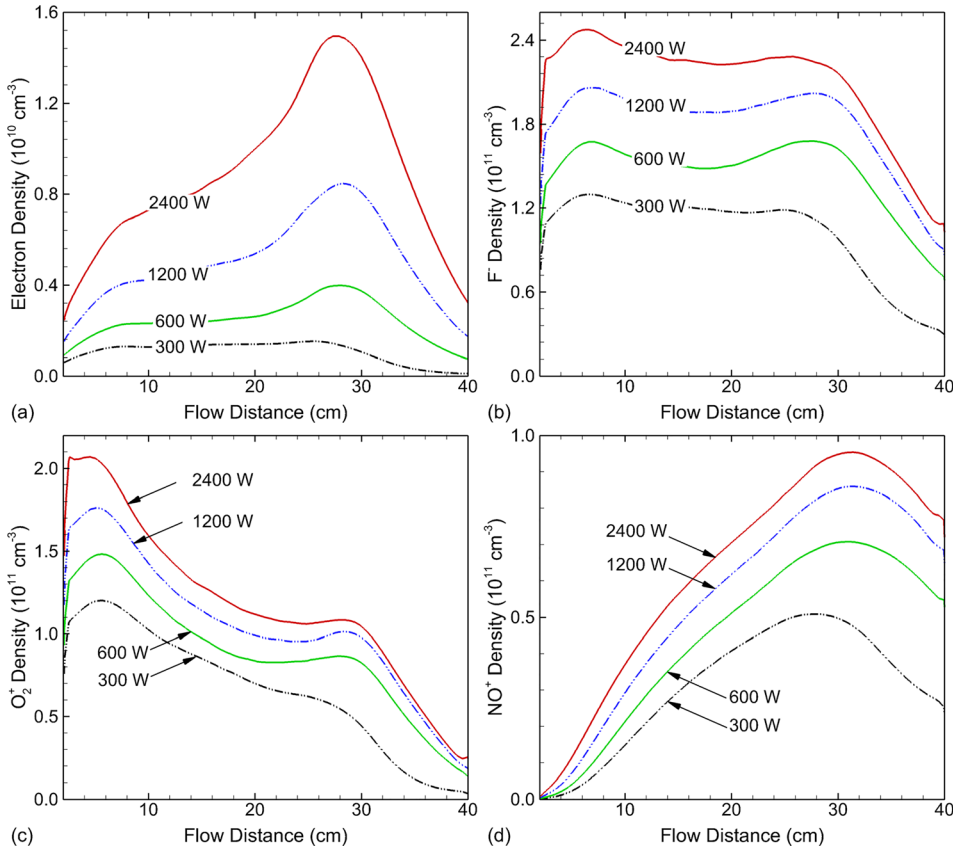

FIG. 16. (Color online) Densities of (a) electrons, (b) F^-, (c) O_2^+, and (d) NO^+ ions along the central axial flow distance in a remote plasma source driven by capacitively coupled power of 300, 600, 1200, and 2400 W. Discharge conditions: $Ar/NF_3/O_2 = 5/10/100$, 400 mTorr, 1150 sccm, 300–2400 W, and 10 MHz.

Since the precursors for these reactions are produced near the sheath edge, the densities of FNO and NO_2 are enhanced near the electrodes.

Downstream of the electrodes, the densities of most neutral species rebound due to the cooling of the gas from 670 to 610 K by thermal conduction to the walls, a similar trend as predicted by the global model. T_g is maximum in the middle of the gap near the end of the plasma zone, about 5 cm beyond the edge of the electrodes, which can be partially ascribed to axial diffusion and electron dissociative attachment occurring downstream, a process not accounted for in the global model. With this dissociative attachment comes Franck–Condon heating.

When varying power deposition, the relative contributions to ionization by bulk and secondary electrons change due to the apportionment of power between electrons and ions. For example, the S_b and S_s are shown in Fig. 15 for power deposition of 300–2400 W. The corresponding densities of electrons, F^-, O_2^+, and NO^+ at midgap as a function of flow are shown in Fig. 16. The voltage amplitude increases from 630 V (dc bias $= -118$ V) to 1690 V (dc bias $= -498$ V) over this range of power, resulting in large sheath potential and thicker sheath. A larger proportion of the power is then dissipated by ion acceleration in the sheath, which would otherwise reduce ionization. For a factor of 8 increase in power (300–2400 W), the power dissipated by electron collisions increases by only a factor of 2.8 (130–360 W) whereas that for ions increases by a factor of 12 (170–2040 W). However, the energy of secondary electrons emitted from the electrodes increases, which facilitates an increase in S_s above that due to the increase in ion current. For example, S_s increases by an order of magnitude 1.1×10^{15} to $1.0 \times 10^{16}\,cm^{-3}\ s^{-1}$ in the bulk plasma and from 7.9×10^{15} to $2.3 \times 10^{16}\,cm^{-3}\ s^{-1}$ in the sheath with this increase in power.

As the ionization by secondary electrons increases, the plasma responds by allowing more electron loss, which is achieved by lowering T_e and S_b, similar to externally sustained plasmas such as electron beam sustained discharges.[38] As the energy relaxation distance of the high energy secondary electrons is longer than for low energy bulk electrons, S_s is far more uniform across the gap than S_b which responds to the extreme sensitivity of α'. The electron density in the bulk plasma increases from 1.4 to $8.0 \times 10^9\,cm^{-3}$, a larger increase in density than power dissipated by electrons due to the increased efficiency of S_s, The densities of F^-, O_2^+, and NO^+ in the bulk plasma generally increase sublinearly with CCP power, reflecting the smaller increase in ionization processes compared to ion acceleration.

The densities of NF_3, F, and NO, and the gas temperature along the axial flow distance are shown in Fig. 17 for CCP powers of 300–2400 W. The fractional dissociation of NF_3 increases from 9% to 37% and the density of F increases from 1.9 to $3.3 \times 10^{14}\,cm^{-3}$ at the end of the plasma zone

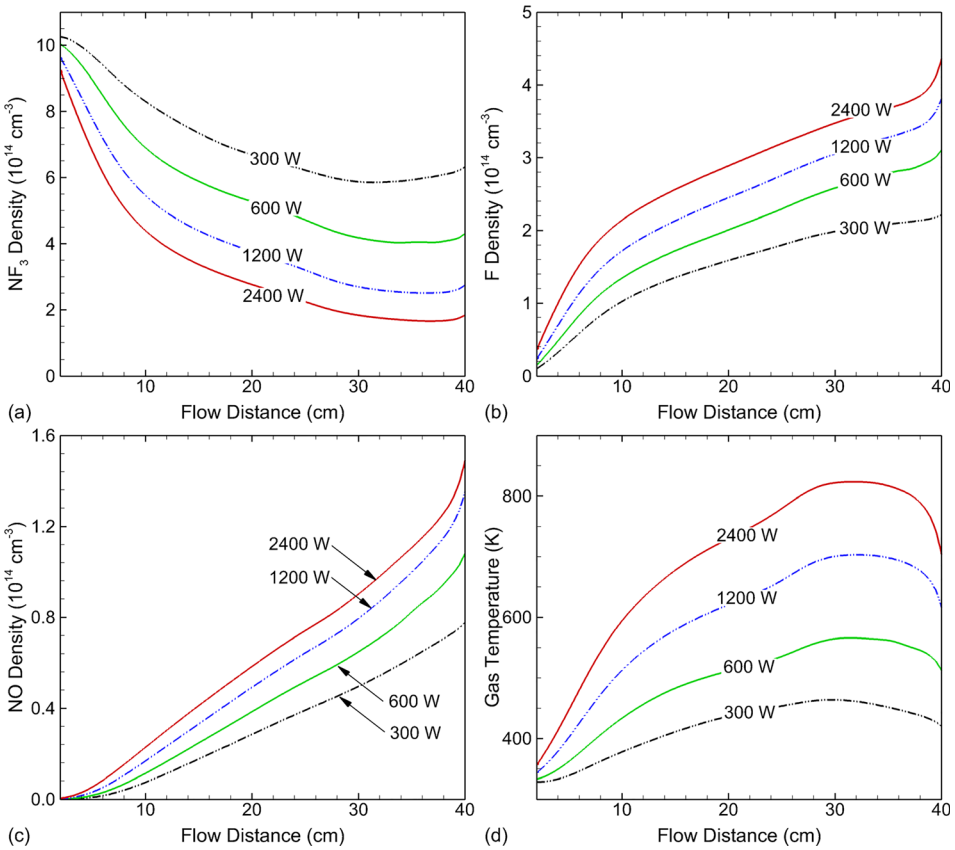

FIG. 17. (Color online) Densities of (a) NF_3, (b) F, (c) NO, and (d) gas temperature along the central axial flow distance in a remote plasma source driven by capacitively coupled power of 300, 600, 1200, and 2400 W. Discharge conditions: $Ar/NF_3/O_2 = 5/10/100$, 400 mTorr, 1150 sccm, 300–2400 W, and 10 MHz.

with increasing power. These increases are significantly less than what might be expected from power deposition alone due to the smaller fraction of power dissipated by electrons and some rarefaction by gas heating. The fractional dissociation of NF_3 predicted by the 2d model is perhaps systematically smaller than predicted by the global model for the same range of power (16%–40%), due to the expansion of the plasma zone beyond the confines of the electrodes. The peak gas temperature increases from 470 K at 300 W to 830 K at 2400 W, and this increase in T_g facilitates the increase in NO density from 4 to $8 \times 10^{13}\,\mathrm{cm}^{-3}$ at the end of the plasma zone due to enhanced endothermic reactions.

VII. CONCLUSION

Global and 2d modeling have been applied to the investigation of remote plasma sources sustained in $Ar/NF_3/O_2$ mixtures. Electron impact cross sections for NF_2 and NF were calculated and a reaction mechanism was developed for plasmas sustained in mixtures containing $Ar/NF_3/O_2$. Overall good agreement was obtained between model predictions and relative densities provided by experimental OES actinometry measurements. In the simulations, NF_x rapidly dissociates in the RPS primarily by dissociative attachment by thermal electrons and secondarily by dissociation due to electronic excitation. The Franck–Condon exothermicity in these dissociative processes is the dominant gas heating mechanism. Addition of O_2 to NF_3 diversifies the variety of radicals (e.g., NO and FNO) and increases radical production. Gas heating aids in the production of NO due to its endothermic formation mechanisms while its loss mechanisms are generally exothermic. The formation of NO is determined by the availability of N_2, which in turn depends on the dissociation of NF_3 to form NF and the recombination probability of N atoms at surface.

Downstream of the plasma zone, the densities of most radicals increase due to gas cooling. However, the density of NF decreases due to exothermic reactions consuming NF and producing N_2 and F_2. In the global model, an ion-ion plasma maintained by $[F^-] \approx [NO^+]$ is formed in the afterglow due to NO having the lowest ionization potential of major species, F having the highest electron affinity, and charge exchange leading to these species. In the 2d model, axial transport and thermal conductivity enable the electron density and sources to extend downstream, which in turn enables an ionization source sustaining O_2^+ downstream and decreased power density. As a result, the fractional dissociation of NF_3 predicted by the 2d model is smaller than the global model and the plasma transitions into a nearly ion-ion plasma with charge neutrality maintained by $[F^-] \approx [NO^+] + [O_2^+]$.

The trends predicted by the global and 2d models generally agree with some exceptions, such as the axial distribution of F atoms, which can be attributed to the spatial distribution of gas temperature and axial diffusion, neither of which are accounted for in the global model. By better confining the plasma in the RPS region through barriers and grids, the efficiency for radical generation can be increased while the plasma will transition into a purely ion–ion plasma, which will lead to increased processing efficiency and less damaging etching downstream.

ACKNOWLEDGMENTS

This work was supported by the Samsung Electronics Co. Ltd., the DOE Office of Fusion Energy Science (DE-SC0001319 and DE-SC0014132) and the National Science Foundation (CHE-1124724 and PHY-1500126).

[1]V. M. Donnelly and A. Kornblit, J. Vac. Sci. Technol. A **31**, 050825 (2013).
[2]S. Fujimura, K. Shinagawa, M. Nakamura, and H. Yano, Jpn. J. Appl. Phys. **29**, 2165 (1990).
[3]B. Thedjoisworo, D. Cheung, and V. Crist, J. Vac. Sci. Technol. B **31**, 021206 (2013).
[4]B. E. E. Kastenmeier, P. J. Matsuo, J. J. Beulens, and G. S. Oehrlein, J. Vac. Sci. Technol. A **14**, 2802 (1996).
[5]B. E. E. Kastenmeier, P. J. Matsuo, G. S. Oehrlein, and J. G. Langan, J. Vac. Sci. Technol. A **16**, 2047 (1998).
[6]Y. B. Yun, S. M. Park, D. J. Kim, N.-E. Lee, C. K. Choi, K. S. Kim, and G. H. Bae, Thin Solid Films **516**, 3549 (2008).
[7]W. Heo, J. H. Ahn, and N.-E. Lee, J. Vac. Sci. Technol. A **28**, 1073 (2010).
[8]D. J. Kim, Y. B. Yun, J. Y. Hwang, N.-E. Lee, K. S. Kim, and G. H. Bae, Microelectron. Eng. **84**, 560 (2007).
[9]E. Meeks, R. S. Larson, S. R. Vosen, and J. W. Shon, J. Electrochem. Soc. **144**, 357 (1997).
[10]S. R. Vosen, E. Meeks, R. S. Larson, and J. W. Shon, J. Electrochem. Soc. **144**, 1514 (1997).
[11]S. P. Gangoli, A. D. Johnson, A. A. Fridman, R. V. Pearce, A. F. Gutsol, and A. Dolgopolsky, J. Phys. D: Appl. Phys. **40**, 5140 (2007).
[12]J.-S. Chang, K. G. Kostov, K. Urashima, T. Yamamoto, Y. Okayasu, T. Kato, T. Iwaizumi, and K. Yoshimura, IEEE Trans. Ind. Appl. **36**, 1251 (2000).
[13]H. L. Chen, H. M. Lee, and M. B. Chang, Plasma Processes Polym. **3**, 682 (2006).
[14]T. Kimura and K. Hanaki, Jpn. J. Appl. Phys. **47**, 8546 (2008).
[15]A. M. Lietz and M. J. Kushner, J. Phys. D: Appl. Phys. **49**, 425204 (2016).
[16]S. D. Rockwood, Phys. Rev. A **8**, 2348 (1973).
[17]M. J. Kushner, J. Phys. D: Appl. Phys. **42**, 194013 (2009).
[18]V. Lisovskiy, V. Yegorenkov, P. Ogloblina, J.-P. Booth, S. Martins, K. Landry, D. Douai, and V. Cassagne, J. Phys. D: Appl. Phys. **47**, 115203 (2014).
[19]J. Tennyson, Phys. Rep. **491**, 29 (2010).
[20]NIST, "Computational chemistry comparison and Benchmark database," http://cccbdb.nist.gov/alldata2x.asp.
[21]NIST, "Chemistry webbook," http://webbook.nist.gov/cgi/cbook.cgi?ID=C7783542&Mask=1EFF.
[22]Y.-K. Kim, Phys. Rev. A **64**, 032713 (2001).
[23]J. R. Hamilton, T. Tennyson, S. Huang, and M. J. Kushner, "Calculated cross sections for electron collisions with NF_3, NF_2 and NF with applications to remove plasma sources," Plasma Sources Sci. Technol. (submitted).
[24]P. Tian and M. J. Kushner, Plasma Sources Sci. Technol. **24**, 034017 (2015).
[25]D. S. Stafford and M. J. Kushner, J. Appl. Phys. **96**, 2451 (2004).
[26]W. Tian, K. Tachibana, and M. J. Kushner, J. Phys. D: Appl. Phys. **47**, 055202 (2014).
[27]N. A. Dyatko, Y. Z. Ionikh, I. V. Kochetov, D. L. Marinov, A. V. Meshchanov, A. P. Napartovich, F. B. Petrov, and S. A. Starostin, J. Phys. D **41**, 055204 (2008).
[28]Y. Ikezoe, S. Matsuoka, M. Takebe, and Viggiano, *Gas Phase Ion Molecule Reaction Rate Constants Through 1986* (Ion Reaction Research Group of the Mass Spectroscopy Society of Japan, Tokyo, Japan, 1987).
[29]R. E. Olson, J. R. Peterson, and J. Moseley, J. Chem. Phys. **53**, 3391 (1970).
[30]T. M. Miller, N. S. Shuman, and A. A. Viggiano, J. Chem. Phys. **136**, 204306 (2012).
[31]N. Ruckhaberle, L. Lehmann, S. Matejcik, E. Illenberger, Y. Bouteiller, V. Periquet, L. Museur, C. Desfrançois, and J.-P. Schermann, J. Phys. Chem. A **101**, 9942 (1997).

[32]M. Bettendroff and S. D. Peyerimhoff, Chem. Phys. **99**, 55 (1985).
[33]R. A. Gottscho and V. M. Donnelly, J. Appl. Phys. **56**, 245 (1984).
[34]J.-s. Jenq, J. Ding, J. W. Taylor, and N. Hershkowitz, Plasma Sources Sci. Technol. **3**, 154 (1994).
[35]D. R. Boris, T. B. Petrova, G. M. Petrov, and S. G. Walton, J. Vac. Sci. Technol. A **35**, 01A104 (2017).
[36]D. V. Lopaev, A. V. Volynets, S. M. Zyryanov, A. I. Zotovich, and A. T. Rakhimov, J. Phys. D: Appl. Phys. **50**, 075202 (2017).
[37]K. J. Nordheden and J. T. Verdeyen, J. Electrochem. Soc. **133**, 2168 (1986).
[38]R. J. Commisso, R. F. Fernsler, V. E. Scherrer, and I. M. Vitkovitsky, IEEE Trans. Plasma Sci. **10**, 241 (1982).
[39]G. Bekefi, *Principles of Laser Plasmas* (John Wiley & Sons, New York, 1976).
[40]M. Hayashi and T. Nimura, J. Appl. Phys. **54**, 4879 (1983).
[41]W. L. Morgan, "Kinema research and software," http://www.kinema.com.
[42]G. Bekefi, *Radiation Processes in Plasmas* (John Wiley & Sons, New York, 1966).
[43]L. Josić, T. Wróblewski, Z. L. Petrović, J. Mechlińska-Drewko, and G. P. Karwasz, Chem. Phys. Lett. **350**, 318 (2001).
[44]D. Rapp and D. D. Briglia, J. Chem. Phys. **43**, 1480 (1965).
[45]B. G. Lindsay, M. A. Mangan, H. C. Straub, and R. F. Stebbings, J. Chem. Phys. **112**, 9404 (2000).
[46]Y. Sakai, T. Okumura, and H. Tagashira, Aust. J. Phys. **48**, 419 (1995).
[47]M. Hayashi and A. Niwawi, *Gaseous Dielectrics V*, edited by L. G. Christophorou and D. W. Bouldin (Pergamon, New York, 1987), pp. 27–32.
[48]L. E. Kline, W. D. Partlow, R. M. Young, R. R. Mitchell, and T. V. Congedo, IEEE Trans. Plasma Sci. **19**, 278 (1991).
[49]D. L. Huestis, R. M. Hill, H. H. Nakano, and D. C. Lorents, J. Chem. Phys. **69**, 5133 (1978).
[50]K. Sasaki, Y. Kawai, and K. Kadota, Rev. Sci. Instrum. **70**, 76 (1999).
[51]L. G. Piper, J. Chem. Phys. **97**, 270 (1992).
[52]B. Gordiets, C. M. Ferreira, M. J. Pinheiro, and A. Ricard, Plasma Sources Sci. Technol. **7**, 363 (1998).
[53]R. Atkinson, D. L. Baulch, R. A. Cox, R. F. Hampson, J. A. Kerr, M. J. Rossi, and J. Troe, J. Phys. Chem. Ref. Data **26**, 521 (1997).
[54]J. T. Herron and D. S. Green, Plasma Chem. Plasma Process. **21**, 459 (2001).
[55]V. G. Anicich, J. Phys. Chem. Ref. Data **22**, 1469 (1993).
[56]P. K. Leichner and R. J. Ericson, Phys. Rev. A **9**, 251 (1974).
[57]E. E. Ferguson, Adv. Electron. Electron Phys. **24**, 1 (1968).
[58]Y. Sakiyama, D. B. Graves, H.-W. Chang, T. Shimizu, and G. E. Morfill, J. Phys. D: Appl. Phys. **45**, 425201 (2012).
[59]W. Van Gaens and A. Bogaerts, J. Phys. D: Appl. Phys. **46**, 275201 (2013).
[60]R. Johnsen and M. A. Biondi, J. Chem. Phys. **73**, 5045 (1980).
[61]B. F. Gordiets, C. M. Ferreira, V. L. Guerra, J. M. A. H. Loureiro, J. Nahorny, D. Pagnon, M. Touzeau, and M. Vialle, IEEE Trans. Plasma Sci. **23**, 750 (1995).
[62]P. B. Armentrout, D. W. Berman, and J. L. Beauchamp, Chem. Phys. Lett. **53**, 255 (1978).
[63]M. Touzeau, G. Gousset, J. Jolly, D. Pagnon, M. Vialle, C. M. Ferreira, J. Loureiro, M. Pinheiro, and P. A. Sá, "Spectroscopy and kinetics of an oxygen glow discharge," *Nonequilibrium in Partially Ionized Gases*, edited by M. Capitelli and J. M. Bardsley (Plenum, New York, 1990), pp. 571–580.
[64]J. I. Steinfeld, S. M. Adler-Golden, and J. W. Gallagher, J. Phys. Chem. Ref. Data **16**, 911 (1987).
[65]R. B. Norton, E. E. Ferguson, F. C. Fehsenfeld, and A. L. Schmeltekopf, Planet. Space Sci. **14**, 969 (1966).
[66]M. McFarland, D. L. Albritton, F. C. Fehsenfeld, E. E. Ferguson, and A. L. Schmeltekopf, J. Chem. Phys. **59**, 6629 (1973).
[67]R. M. Snuggs, D. J. Volz, I. R. Gatland, J. H. Schummers, D. W. Martin, and E. W. McDaniel, Phys. Rev. A **3**, 487 (1971).
[68]F. C. Fehsenfeld, D. L. Albritton, J. A. Burt, and H. I. Schiff, Can. J. Chem. **47**, 1793 (1969).
[69]C. Lifshitz, R. L. C. Wu, T. O. Tiernan, and D. T. Terwilliger, J. Chem. Phys. **68**, 247 (1978).
[70]S. W. Benson and A. E. Axworthy, J. Chem. Phys. **26**, 1718 (1957).
[71]E. Meeks, S. R. Vosen, J. W. Shon, R. S. Larson, C. A. Fox, and D. Buchenauer, "Results from modeling and simulation of chemical downstream etch systems," Sandia Report, Report No. SAND96-8241 (1996).
[72]R. Atkinson, D. L. Baulch, R. A. Cox, R. F. Hampson, J. A. Kerr, M. J. Rossi, and J. Troe, J. Phys. Chem. Ref. Data **26**, 1329 (1997).
[73]J. A. Kerr and S. J. Moss, *CRC Handbook of Bimolecular and Termolecular Gas Reactions* (CRC, Boca Raton, FL, 1981).
[74]G. London, R. Gilpin, H. I. Schiff, and K. H. Welge, J. Chem. Phys. **54**, 4512 (1971).
[75]A. F. Trotman-Dickenson and G. S. Milne, *Tables of Bimolecular Gas Reactions (NSRDS NBS 9)* (U.S. Government Printing Office, Washington, DC, 1967).
[76]V. N. Kondratiev, *Rate Constants of Gas Phase Reactions*: *Reference Book* (U.S. Department of Commerce, Springfield, VA, 1972).
[77]I. Shkurenkov, D. Burnette, W. R. Lempert, and I. V. Adamovich, Plasma Sources Sci. Technol. **23**, 065003 (2014).
[78]R. Atkinson, D. L. Baulch, R. A. Cox, R. F. Hampson, J. A. Kerr, and J. Troe, J. Phys. Chem. Ref. Data **18**, 881 (1989).
[79]M. Uddi, N. Jiang, I. V. Adamovich, and W. R. Lempert, J. Phys. D: Appl. Phys. **42**, 075205 (2009).
[80]L. J. Stief, W. A. Payne, J. H. Lee, and J. V. Michael, J. Chem. Phys. **70**, 5241 (1979).
[81]M. Gonzalez, I. Miquel, and R. Sayos, Chem. Phys. Lett. **335**, 339 (2001).
[82]J. W. Duff and R. D. Sharma, Geophys. Res. Lett. **23**, 2777, doi:10.1029/96GL02613 (1996).
[83]J. C. Person and D. O. Ham, Int. J. Radiat. Appl. Instrum. Part C. Radiat. Phys. Chem. **31**, 1 (1988).
[84]R. A. Young, G. Black, and T. G. Slanger, J. Chem. Phys. **49**, 4758 (1968).
[85]R. Atkinson, D. L. Baulch, R. A. Cox, J. N. Crowley, R. F. Hampson, R. G. Hynes, M. E. Jenkin, M. J. Rossi, and J. Troe, Atmos. Chem. Phys. **4**, 1461 (2004).
[86]M. Gonzalez, R. Sayos, and R. Valero, Chem. Phys. Lett. **355**, 123 (2002).
[87]R. Atkinson, D. L. Baulch, R. A. Cox, R. F. Hampson, J. A. Kerr, and J. Troe, J. Phys. Chem. Ref. Data **21**, 1125 (1992).
[88]I. C. Plumb and K. R. Ryan, Plasma Chem. Plasma Process. **6**, 205 (1986).
[89]P. R. P. Barreto, A. F. A. Vilela, R. Gargano, S. S. Ramalho, and L. R. Salviano, J. Mol. Struct. THEMCHEM **769**, 201 (2006).
[90]C. T. Cheah, M. A. A. Clyne, and P. D. Whitefield, J. Chem. Soc. Faraday Trans. II **76**, 711 (1980).
[91]V. B. Rozenshtein, Y. R. Bedzhanyan, and Y. M. Gershenzon, Kinet. Catal. **29**, 22 (1988).
[92]J. T. Herron, J. Phys. Chem. Ref. Data **28**, 1453 (1999).
[93]B. H. Weiller, R. F. Heidner, J. S. Holloway, and J. B. Koffend, J. Phys. Chem. **96**, 9321 (1992).
[94]W. Corbin and J. B. Levy, Int. J. Chem. Kinet. **7**, 679 (1975).
[95]J. B. Levy and B. K. W. Copeland, J. Phys. Chem. **69**, 3700 (1965).
[96]V. I. Sorokin, N. P. Gritsan, and A. I. Chichinin, J. Chem. Phys. **108**, 8995 (1998).
[97]Y. R. Bedzhanyan, Y. M. Gershenzon, and V. B. Rozenshtein, Kinet. Catal. **31**, 1291 (1990).
[98]Y. G. Bedzhanyan, Y. M. Gershenson, S. D. Il'in, O. P. Kishkovic, and V. B. Rozenshtein, Sov. J. Chem. Phys. **6**, 610 (1990).
[99]A. A. Turnipseed and J. W. Birks, J. Phys. Chem. **95**, 6569 (1991).
[100]T. J. Wallington, W. F. Schneider, J. J. Szente, M. M. Maricq, O. J. Nielsen, and J. Sehested, J. Phys. Chem. **99**, 984 (1995).
[101]A. C. Lloyd, Int. J. Chem. Kinet. **3**, 39 (1971).
[102]F. Westley, J. H. Herron, and R. J. Cvetanovic, *Compilation of Chemical Kinetic Data for Combustion Chemistry (NSRDS-NBS 73, Parts 1 and 2)* (U.S. Government Printing Office, Washington, DC, 1987).
[103]K. Thielen and P. Roth, AIAA J. **24**, 1102 (1986).
[104]V. M. Doroshchenko, N. N. Kudriavtsev, A. M. Sukhov, and D. P. Shamshev, Chem. Phys. Lett. **193**, 258 (1992).
[105]D. L. Baulch, J. Duxbury, S. J. Grant, and D. C. Montague, J. Phys. Chem. Ref. Data **10**, 1 (1981).
[106]W. Tsang and J. T. Herron, J. Phys. Chem. Ref. Data **20**, 609 (1991).
[107]D. R. F. Burgess, M. R. Zachariah, W. Tsang, and P. R. Westmoreland, Prog. Energy Combust. Sci. **21**, 453 (1995).
[108]M. Matti Maricq, J. J. Szente, T. S. Dibble, and J. S. Francisco, J. Phys. Chem. **98**, 12294 (1994).
[109]J. B. Koffend, C. E. Gardner, and R. F. Heidner III, J. Chem. Phys. **83**, 2904 (1985).